ULTRAVIOLET-ASSISTED PROCESSING OF DIELECTRIC THIN FILMS FOR METAL OXIDE SEMICONDUCTOR APPLICATIONS

By

JOSHUA M. HOWARD

A DISSERTATION PRESENTED TO THE GRADUATE SCHOOL
OF THE UNIVERSITY OF FLORIDA IN PARTIAL FULFILLMENT
OF THE REQUIREMENTS FOR THE DEGREE OF
DOCTOR OF PHILOSOPHY

UNIVERSITY OF FLORIDA

2002

Copyright 2002

by

Joshua M. Howard

I would like to dedicate this work to the memory of my great grandmother, mormor, who will live on in my heart forever.

ACKNOWLEDGMENTS

I would like to first thank my advisor, Dr. Rajiv Singh, for all the enduring support and encouragement he has given to me since I joined his group. His guidance and friendship have played an integral role in molding me into the scientific researcher I am today. Next I would like to thank Dr. Valentin Cracuin, who also works with Dr. Singh as a visiting researcher from Romania. Valentin has acted as a great mentor throughout my time here. He has served as an inspiration for me to excel in all aspects of any project I undertake and taught me to look deeper than what may appear on the surface. Above all, Valentin has become someone whom I can truly call my friend. I would also like to thank Dr. Stephen Pearton for serving on my committee and for his keen insight into life that has always helped me put the world into perspective. I would also like to thank Dr. Cammy Abernathy for her smile and kind word that has often helped me through the day. Additionally, I thank Dr. David Norton for his assistance, enthusiasm, and for use of his laboratory equipment. Finally I would like to thank Dr. Fan Ren for use of his electrical characterization equipment and for serving on my committee.

I would like to thank my parents, my brother David, and my extended family for all of the love and encouragement they have given me throughout my life. I will always cherish the active roles each played in my life growing up and how each person worked in a special way to help me become the person I am today.

There are many contemporaries here at the University of Florida that deserve thanks for their help and friendship. In particular, I would like to thank Brent Gila, Mark

Overberg, Michael Ollinger, Nabil Bassim, Francis Kelly, Anuranjan Srivastava, Srinivas Pietambaram, Chad Essary, and Seemant Rawal. I would also like to acknowledge all of the other wonderful group members current and past that are far too many to list.

There are many friends that have come and gone throughout my life, but occasionally you meet people who you know will be there for the rest of your life. I would like to thank several of my dear high school friends, including Christopher Schmidt, Andrew Rogers, the whole Coombs clan, and Victoria Aronold, for all of their love, lessons, and friendship. I would also like to thank Daniel Kammler from my days at the University of Missouri-Rolla for being a truly amazing human being.

Additionally, I would like to thank my best friend Jennifer Gray for all of her love and care. It is not every day that you get to be best friends with the person you love, but somehow I have found myself in this situation. Her confidence and spirit make my world a happier place to live. I thank her for everything that she is.

It would be impossible to list all of the attributes that each of these close friends exhibits, but it can definitely be summed up that these people represent the best that the human race has to offer and for this I feel blessed that they have been a part of my life.

TABLE OF CONTENTS

page

ACKNOWLEDGMENTS iv

ABSTRACT xiv

CHAPTER

1 LITERATURE REVIEW 1

Introduction 1
The Transistor 1
History 2
Basic Transistor 2
Fundamental Limitations 3
Materials Selection Criteria 4
Permittivity and Barrier Height 5
Thermodynamic Stability 5
Interface Quality 6
Film Microstructure 7
Gate Compatibility 7
Process Compatibility 8
Reliability 8
Excimer Laser Basics 9
Ultraviolet Lamp Basics 10
Ultraviolet Excimer Radiation Sources 10
Silent Barrier Discharge Excimer Radiation 11
Materials and Properties 13
Motivation 15
Oxygenation of Films 18

2 EXPERIMENTAL PROCEDURES 27

System Geometries 27
Laser System 27
UVPLD System 29
Excimer Annealing System 30
Excimer Lamp Design 30
Experimental Setups and Samples 31
Interfacial Layer Formation 32

In-Situ Ultraviolet PLD 32
Post Deposition Ultraviolet Annealing 33
Experimental Characterization Techniques 34
Variable Angle Spectroscopic Ellipsometry 34
X-ray Reflectivity 35
X-ray Diffraction and Glancing Incidence X-ray Diffraction 36
X-ray Photoelectron Spectroscopy 38
Atomic Force Microscopy 38
Fourier Transform Infrared Spectroscopy 39
Electrical Characterization 39
Current-Voltage Measurements 40
Capacitance-Voltage Measurement 41
Transmission Electron Microscopy 45

3 INTERFACIAL LAYER FORMATION 59

Anneal Conditions 59

4 ULTRAVIOLET PROCESSING 81

In-situ Ultraviolet PLD 81
Barium Strontium Titanate (BST) 82
Yttrium Oxide (Y_2O_3) 90

5 POST DEPOSITION ULTRAVIOLET ANNEALING 105

Ultraviolet-Assisted Oxidation of Silicon 105
HfO_2 Post Deposition Anneal 106

6 CONCLUSIONS 117

APPENDIX ELECTRICAL DATA EXTRACTION METHOD 120

LIST OF REFERENCES 125

BIOGRAPHICAL SKETCH 129

LIST OF TABLES

Table		page
1-1	Industrial timeline for minimum feature size and equivalent dielectric thickness in MOSFET devices [2].	4
1-2	Different wavelengths possible as a function of rare gas or rare gas halide mixture used for excimer decomposition.	14
1-3	Various properties of high-k oxide materials	15
2-1	Conditions for growth and post deposition heat treatments of thin ZrO_2 films	32
2-2	Conditions for in-situ ultraviolet annealing with an Hg lamp array during growth of BST and Y_2O_3 thin films.	33
2-3	Conditions for post deposition excimer anneals of HfO_2 thin films	34
2-4	Conversion factors for series-parallel electrical equivalent circuits.	44
3-1	Partial pressure of oxygen for respective deposition ambients	60
3-2	VASE thickness measurements of ZrO_2 samples after post-deposition heat teatments in various ambients.	61
3-3	Thickness, roughness, and density data for the various XRR model options for the oxygen annealed ZrO_2	62
3-4	Modeling data for the as-deposited, vacuum, helium, and oxygen annealed samples.	63
4-1	XRR data for the PLD and UVPLD deposited BST samples.	83
4-2	XRD peak data for the PLD and UVPLD deposited BST samples.	85
4-3	GIXD peak data for the PLD and UVPLD deposited BST samples:	86
4-4	XRR data for the PLD and UVPLD deposited Y_2O_3 samples.	91
4-5	GIXD peak data for the PLD and UVPLD deposited Y_2O_3 samples	92

5-1 VASE thickness measurements for silicon oxidized with and without ultraviolet radiation at 300°C. 106

5-2 VASE thickness measurements for HfO_2 anneals with and without ultraviolet radiation. 108

5-3 XRR data for the thickness and density of the amorphous interfacial layer..... 109

LIST OF FIGURES

Figure page

1-1 Schematic of a typical MOSFET. The gate, insulator, and silicon form the metal oxide semiconductor capacitor portion of a MOSFET 21

1-2 Calculated conduction and valence band offsets for various perspective alternative dielectric materials on Si 22

1-3 Ternary phase diagrams illustrating a) "SiO_2 dominant," b) "no phase dominant," and c) "metal oxide dominant" systems. System c represents a stable condition for a metal oxide when in direct contact with silicon 23

1-4 Schematic of total energy associated with laser ablation of a surface. 24

1-5 Sinusoidal voltage versus time plot indicating conditions where silent barrier microdischarges may occur 25

1-6 Spectral emission characteristics for A) low pressure mercury lamp and B) xenon excimer lamp 26

2-1 Ultraviolet-assisted pulsed laser deposition system, KrF excimer laser, and optic setup. 46

2-2 Homemade excimer annealing system equipped with vacuum ultraviolet lamp 47

2-3 Schematic of excimer lamp illustrating the concentric tube design and how a radio frequency load is delivered to the system. 48

2-4 Tiny microdischarges from the ignited excimer lamp are the origin of the excimer radiation. 49

2-5 General x-ray reflectivity setup showing physical relationships between the acquired data and the modeling output. 50

2-6 General x-ray diffraction setup illustrating the interaction of x-rays with a structure as they pertain to Braggs Law 51

2-7 Process of incoming radiation ejecting a characteristic photoelectron from a carbon sample 52

2-8 Schematic of atomic force microscope and the various components that allow up to atomic resolution....53

2-9 Typical MOS capacitor prepared for this dissertation....54

2-10 Block diagram of Keithley Win-82 system and how it connects to the probe station. Adapted from Keithley Win-82 operation manual....55

2-11 Typical capacitance-voltage illustrating the three main regions that occur in a MOS device as a function of bias voltage applied. Adapted from the Keithley Win-82 operation manual....56

2-12 A) parallel, B) series, and C) combined series and parallel models for generation of capacitance information....57

2-13 Schematic of electron beam after passing through an ultrathin TEM sample. Some electrons are scattered while others remain unscattered....58

3-1 XRR spectra of A) raw data, B) 1 layer model without fit, C) 1 layer model with fit, and D) 2 layer model with fit illustrating the importance of a good model when analyzing XRR data....71

3-2 XRR spectra of A) as-deposited, B) vacuum annealed, C) helium annealed, and D) oxygen annealed ZrO_2 thin films as modeled with the "2 layer model with fit"..72

3-3 Plot of interfacial layer density as determined by XRR as a function of oxygen content in the annealing system. Bulk SiO_2 has been added as a reference....73

3-4 Cross sectional TEM of a polycrystalline ZrO_2 thin film atop an amorphous interfacial layer atop single crystalline silicon....74

3-5 FTIR spectra of A) oxygen anneal, B) helium anneal, and C) as-deposited ZrO_2 thin films showing the increase in Si—O bonding absorption in stretching, bending and rocking modes....75

3-6 XPS data of Si 2p region of an as-deposited ZrO_2 thin film and after various post deposition anneals....76

3-7 Plot of Si 2p binding energy of oxygen bonded to silicon as a function of oxygen content in the annealing system. Bulk SiO_2 has been added as a reference....77

3-8 XPS spectra of A) raw data, B) 1 peak fit, C) 2 peak fit, and D) 3 peak fit fit illustrating the importance of a good model when analyzing XPS data....78

3-9 XPS spectra with "3 peak fit" of A) as-deposited, B) vacuum annealed, C) helium annealed, and D) oxygen annealed ZrO_2....79

3-10 Plot of O 1s binding energy of oxygen bonded to silicon as a function of oxygen content in the annealing system. Bulk SiO_2 has been added as a reference. 80

4-1 XRR spectra of A) UVPLD raw data, B) UVPLD 1 layer model, C) UVPLD 3 layer model, and D) PLD 3 layer model for BST samples. 94

4-2 Cross sectional TEM of a polycrystalline BST thin film atop an amorphous interfacial layer atop a single crystal silicon substrate.....95

4-3 AFM of BST for PLD and UVPLD deposited samples. The UVPLD deposited sample exhibits increased roughness larger grain sizes.....96

4-4 GIXD of BST for PLD and UVPLD deposited samples. The UVPLD deposited sample exhibits increased (110) texturing. 97

4-5 O 1s XPS of BST for PLD and UVPLD deposited samples. Peak B corresponds to the amount of physically trapped oxygen in the thin film structure and is reduced in the UVPLD deposited sample.....98

4-6 Current density versus voltage plot for BST of PLD and UVPLD deposited samples.....99

4-7 High frequency capacitance versus voltage plot for BST of PLD and UVPLD deposited samples. 100

4-8 XPS spectra of A) UVPLD raw data, B) UVPLD 3 layer model, C) PLD raw data, and D) PLD 3 layer model for Y_2O_3 samples.....101

4-9 Cross sectional TEM of a polycrystalline Y_2O_3 thin film atop an amorphous interfacial layer atop a single crystal silicon substrate.....102

4-10 GIXD of Y_2O_3 for PLD and UVPLD deposited samples. The UVPLD sample exhibits increased (222) texturing.....103

4-11 O 1s XPS of Y_2O_3 for PLD UVPLD deposited samples. Peak B corresponds to the amount of physically trapped oxygen within the thin film structure. 104

5-1 VASE thickness versus time results for oxidation of silicon with and without excimer radiation in oxygen.....112

5-2 VASE thickness of the overall HfO_2 for samples annealed with and without utraviolet radiation. 113

5-3 XRR thickness measurements of the HfO_2 interfacial layer for samples annealed with and without ultraviolet radiation.....114

5-4 XRR density measurements of the HfO_2 interfacial layer for samples annealed with and without ultraviolet radiation.....115

5-5 Capacitance-voltage measurements of HfO_2 MOS devices for samples annealed with and without ultraviolet radiation.....116

Abstract of Dissertation Presented to the Graduate School
of the University of Florida in Partial Fulfillment of the
Requirements for the Degree of Doctor of Philosophy

ULTRAVIOLET-ASSISTED PROCESSING OF
DIELECTRIC THIN FILMS FOR METAL OXIDE
SEMICONDUCTOR APPLICATIONS

By

Joshua M. Howard

December, 2002

Chair: Dr. Rajiv K. Singh
Major Department: Materials Science and Engineering

Oxygenation of oxide thin films was studied in this dissertation with application to metal oxide semiconductor technology. One of the main challenges envisioned for future microelectronic devices is finding a replacement gate dielectric for silicon dioxide (SiO_2) on silicon in metal oxide semiconductor applications. Several alternative high-k dielectric materials have been proposed as a solution to this problem because insertion of such a layer would allow thicker layers not subject to tunneling leakage issues encountered with ultrathin SiO_2 layers to be deposited. However, studies have indicated that new problems exist with these alternative layers. Among these issues are the formation of a low-k interfacial dielectric layer and an unacceptable level of oxygen vacancies in the films that contribute to leakage currents. In an attempt to address these issues, a three part experimental procedure has been designed to look at the role of oxygen in the thin film system. First, the formation of an interfacial layer as a function of

oxygen concentration in the thin film system has been investigated. Next, ultraviolet radiation was added to a pulsed laser deposition (PLD) system for in-situ ultraviolet-assisted PLD growth of dielectric films. Through the addition of ultraviolet radiation, highly reactive oxygen species are generated which alter the oxygenation conditions and dynamically alter the films properties and final oxygenation conditions. Finally, the application of ultraviolet annealing to already deposited hafnium dioxide (HfO_2) thin films was studied to look at the possibility of more fully oxygenating the film after growth. A variety of characterization techniques indicate that both oxygen trapped in the film and oxygen that passes from the ambient through the film to the interface are responsible for the formation of the interfacial layer. Additionally, the application of ultraviolet radiation to a growth system can alter physical properties of a growing film, such as texturing of a polycrystalline film and overall reduction of trapped oxygen within the film. Furthermore, post-deposition ultraviolet annealing allows for the migration of oxygen species to the interface for growth of the interface and results in an unwanted reduction of the overall electrical properties.

CHAPTER 1
LITERATURE REVIEW

Introduction

Although silicon dioxide has remained the insulator of choice in metal oxide semiconductor devices for more than three decades, fundamental limitations of the material predict that its reign will soon come to an end. This has prompted many research teams around the world to search for a solution to this problem. However, the answer has proven to be surprisingly elusive. An approach chosen by many is to use a high dielectric constant material in place of the SiO_2 layer, thus alleviating the issues that are forcing the change in the first place. This dissertation addresses problems associated with the implementation of such an alternative layer. Special attention is given to exploring a second unwanted interfacial layer and developing the origins of that layer as a function of oxygen content in the system. Next, the effects of ultraviolet radiation are investigated to determine if a link could be made between the oxygen species in the system and the quality of in-situ and post-deposition processed samples.

The Transistor

The transistor is arguably one of the most important inventions of the twentieth century. It has paved the way for countless technological advancements as humans have moved into an era where communication around the world can occur in a matter of seconds. Data, information, and ideas can stream about the globe without time or distance ever coming into consideration. The transistor, as initially theorized and later

developed, changed the course of computers forever. First it replaced vacuum tubes in early computers, and then was refined to a stage whereby fully integrated circuitry became a reality. Now it is integrated into microprocessors with millions of transistors working flawlessly on a single small microchip. The transistor truly has allowed humans to move into a new definition of existence.

History

In 1945 Bell Laboratories began research into a class of materials known as semiconductors. Their goal was to replace vacuum tubes (developed in 1906) for signal amplification in long distance telecommunications applications. The vacuum tubes were known to be unreliable, consume too much power, and produce too much heat. On December 16th, 1947, the "point contact transistor" was created and consisted of strips of gold foil on a plastic triangle in intimate contact with a slab of germanium. This design was soon improved upon with the invention of the "junction (sandwich) transistor" a year later. This new transistor proved to be more rugged, practical and easier to manufacture. Twelve years later, a new design based on original theories for a field effect transistor was created. This design is the same one that has been continually used and adjusted for the past forty years.

Basic Transistor

A schematic of a modern metal oxide semiconductor field effect transistor (MOSFET) is shown in Figure 1-1 [1]. There are several important features to note. First, the transistor serves as a switching device that works on a field effect theory. As a voltage is applied to the gate, charge carriers from extrinsic dopants in the silicon are either attracted to or repelled from the silicon/silicon dioxide interface. This metal oxide semiconductor (MOS) layered structure is essentially a capacitor. Under certain

conditions the excess charge carriers in the silicon may form a conductive channel at the interface. By sensing whether or not a current is flowing along this channel under certain given conditions, a one and zero interpretation may be generated. For example, if there is a current sensed, a one is interpreted and if no current is sensed, a zero is interpreted. These ones and zeros form the basis of all computer technology, which strings together long arrays of ones and zeros in binary coding.

Fundamental Limitations

To date, the microelectronics industry continues to increase performance by decreasing microelectronic device size. However, several roadblocks have been envisioned for the near future. The desire to increase metal oxide semiconductor field effect transistor (MOSFET) speed by decreasing the lateral dimensions (i.e., gate length) also demands a proportional reduction in the gate oxide thickness. The reduction in gate oxide thickness is necessary in order to maintain a constant capacitance per unit area in the semiconductor material. Within the next several years, silicon dioxide on silicon technology will reach fundamental limitations with respect to unacceptable leakage currents and low breakdown voltages. The problem occurs at very small gate thicknesses (sub 20Å regime) required for future devices because of the exponential dependence of leakage current (due to direct electron tunneling) on the thickness of the dielectric layer [1-3]. Buchanan [2] illustrates the situation for SiO_2, where at a gate bias of ~1 V, the leakage current changes from 1 X 10^{-12} A/cm^2 at ~35Å to 1 A/cm^2 at ~15Å. This represents a change of twelve orders of magnitude in current for a thickness change of little more than a factor of two! This very high leakage current causes many concerns as to the operation of devices with respect to conceivably altering device performance, as well as creating standby power dissipation, reliability, and lifetime issues. As seen in

Table 1-1, the industry timeline as presented by Buchanan [2] for the minimum feature size and the equivalent oxide thickness predicts quickly approaching deadlines for SiO_2 technology.

Table 1-1 Industrial timeline for minimum feature size and equivalent dielectric thickness in MOSFET devices [2].

Year	Minumum Feature Size (μm)	Equivalent Dielectric Thickness (Å)
1997	0.25	40-50
1999	0.18	30-40
2001	0.15	20-30
2003	0.13	20-30
2006	0.10	15-20
2009	0.07	<15
2012	0.05	<10

Though the thinning process has been successful for the past four decades, limits are quickly being approached and must be addressed for the vigorous pace the microelectronic industry has followed for so many years to continue. Bear in mind that this must occur while still maintaining high quality standards that MOSFET technologies require.

Materials Selection Criteria

Due to the problem facing SiO_2 technology, there is a need for an alternate solution for SiO_2 as the dielectric of choice on silicon. However, as mentioned previously, to date, there are no immediate solutions to this problem. Though much work has been done, mainly in the area of high-k dielectric alternatives, incompatibilities with silicon (interfacial layer formation) as well as low quality deposited oxides with high leakage currents and large defect densities have continued to plague the insertion of an alternate layer. As outlined by Wilk et al. [4] in a thorough review of the current status on high-k dielectrics, there are a group of main considerations that must be satisfied before insertion

of an alternate dielectric layer into silicon industrial processes will take place. In short, there are a set of main criteria that must be satisfied for a material to satisfactorily perform as a gate dielectric.

Permittivity and Barrier Height

First, the *permittivity and barrier height* must be taken into consideration. While many scientists originally felt that a material with a $\kappa > 25$ would be necessary, it was later found that this may not be exactly true and that among other things, the barrier height of the material must also be taken into consideration along with the dielectric constant. An example of the band offsets for various high dielectric constant materials in contact with silicon is shown in Figure 1-2 [5]. The best materials for consideration should have a conduction band offset greater than ~1 eV, because as barrier height of the material decreases, there is also an exponential increase in leakage current as a result of Schottky emission of electrons into the conduction band [1, 3]. Unfortunately, there exists a general relationship where barrier height decreases with increasing dielectric constant. A comparison of the band offsets for SiO_2 ($\epsilon = 3.9$) and $BaTiO_3$ ($\epsilon > 2000$) clearly illustrates this point. What this means is that there is an optimization problem to see which will have the larger effect.

Thermodynamic Stability

A second important consideration is the *thermodynamic stability* of the new dielectric material when in direct contact with silicon. An important approach toward predicting and understanding the relative stability of a particular three component system for device applications can be explained through ternary phase diagrams [6]. Hubbard describes the three main categories for phase diagrams as "SiO_2 dominant," "no phase dominant," and "metal oxide dominant." Each of these is shown in Figure 1-3 [6]. The metal oxide

dominant type is of interest in this study. As an example, a comparison of the Zr-Si-O phase diagram (metal oxide dominant) versus the Ta-Si-O (SiO_2 dominant) can reveal a great deal of information. Inspection of the Zr-Si-O phase diagram in Figure 1-3 (C) shows tie lines that directly connect ZrO_2 and Si. This indicates stable ternary compounds (i.e., ZrO_2 should be stable on Si). Though sufficient data are unavailable for the Hf-Si-O system, proximity on the periodic table and in similarities noted between Hf and Zr indicate that the same argument should hold true for the stability of HfO_2 on Si. On the other hand, inspection of the Ta (or Ti) phase diagram in Figure 1-3 (A or B) does not have any tie lines connecting the compound of interest to Si, thus indicating a lack of stable ternary compounds. The stability of the systems, as predicted by these ties lines, is of paramount importance since it suggests that control of the dielectric/Si interface may be possible. However, it is important to keep in mind that even though the phase diagrams indicate stability in certain compounds over others, the phase diagrams are generated for equilibrium conditions. In fact, most of the deposition techniques do not occur under equilibrium conditions. This is an important difference to note since there have been many reports about systems that were predicted to have the thermodynamic considerations under control that still exhibit unwanted interfacial layers [7-10].

Interface Quality

The third criterion that must be considered is the *interface quality*. This is of particular importance because an interface of poor quality will result in degradation of device performance. Imperfect bonding will cause under or overconstrained states that have a direct correlation to the leakage current and electron channel mobility and lead to degraded performance. In addition, a particularly rough interface can have adverse effects on device performance with respect to poor channel mobility characteristics.

Film Microstructure

An additional criterion which has been thoroughly analyzed is the *film microstructure*. There is still much debate on whether a polycrystalline, single crystalline, or amorphous film will work best. It has been argued that a polycrystalline setup is subject to high leakage currents due to nonstoichiometries that occur along the grain boundaries that act as leakage paths. This would seem to infer that a single crystal structure would be an ideal solution to this problem; however, the equipment typically used to grow single crystalline films is very expensive and not readily adaptable to a large scale industrial atmosphere. Furthermore, if it is possible to create a single crystal interface, it is very difficult to maintain the integrity of the single crystalline structure in subsequent thermal processing steps. One may also argue that the amorphous structure of SiO_2 that has been used so successfully for so many years would be ideal. This, however, also runs into problems since many of the high-k dielectric alternatives are not naturally in an amorphous state and quickly convert to a polycrystalline state when subsequent heat treatments of the layer are conducted. This particular concern has been an issue of great debate since many groups have generated decent data for each of the possibilities [11-13].

Gate Compatibility

Next, *gate compatibility* must be taken into consideration. Namely, the dielectric has to be compatible with the current industry standard, which is a highly doped polycrystalline silicon (poly-Si) gate. This proves to be a much greater task than immediately apparent. There are issues associated with the diffusion of the dopant species into the gate dielectric materials, especially such materials as ZrO_2 and HfO_2 that are reported to have rather open structures [2, 5]. The diffusion of the dopant ions into the dielectric may cause deleterious effects on the dielectric properties as well as create areas

in the gate where increased resistances are encountered. There is a possibility of solving this issue by replacing the poly-Si with a metal gate, but there are certain problems associated with that as well. First, the poly-Si gate currently allows tuning of the dopant levels to correlate to desired threshold voltages for both nMOS and pMOS devices. Switching to a metal means that this will no longer be an option, so either a midgap metal or two different metals with appropriate work functions will need to be implemented. It turns out that the midgap metal appears to be potentially limiting due to future predictions of the power requirements versus threshold voltages related to the midgap metal being to large and resulting difficulties turning the devices on. Midgap work function metal gate systems have also been predicted to be unable to provide a performance improvement worthy of the added process complexity [4]. This leaves the option of introducing two different metals into the CMOS system. Though this would require a bit of additional work to fully investigate the associated issues, this does appear to be a viable option for future devices.

Process Compatibility

Next, it is important to ensure that the dielectric does have good *process compatibility*. Simply stated, the microelectronics industry is tooled for large scale fabrication of SiO_2 on silicon devices. It is easily conceivable that the dielectric that most easily slips into the current complex industrial process or requires the fewest number of modifications will be chosen. This is regardless of its status in other areas so long as continued device performance can still be achieved.

Reliability

Finally, the reliability of devices must be proven. Time dependent dielectric breakdown studies where higher voltages stress devices to breakdown conditions in

reasonable time periods so that lifetime estimates for actual working conditions may be calculated must be conducted. Once done, the lifetime calculations must fit into the stringent ten year lifetime policy set up as the industry standard. To date, few reports have been generated of this nature and additional work must still be conducted.

Excimer Laser Basics

Though there are many techniques available for the deposition of thin oxide films onto a substrate, pulsed laser deposition has several key advantages that make it an ideal research tool. Stoichiometric transfer of molecules from the target to the substrate, effective rapid prototyping of many different materials, and a wide range of applications are foremost on this list.

The ablation process itself is characterized by an input of energy from the laser to a given target material. Subsequently, the energy distribution shown in Figure 1-4 [14] occurs whereby the total energy for the system is represented as

$$E = E_r + E_p + E_d + E_c \qquad (1\text{-}1)$$

where E is the laser energy, E_r the reflected energy, E_p the energy of the plasma plume, E_d the energy of disintegration due to particles blown off by the vapor-gas jet, and E_c the energy absorbed by the cavity wall. There are additional factors related to the laser energy that play an important role in surface response to pulse energy. For a given material, a combination of pulse energy and ablation threshold energy determines if ablation will occur, and to what level. It should be apparent that higher pulse energies result in an increasing level of ablation. If the pulse energy is less than the ablation threshold, material will not be physically removed from the surface (i.e., Ep and Ed tend to zero), but that energy may still be absorbed by the cavity wall (Ec) for laser annealing

experiments. All experimentation in this study was carried out at an energy value much greater than the ablation threshold.

Ultraviolet Lamp Basics

Ultraviolet Excimer Radiation Sources

Over the past decade, numerous research teams have placed a considerable amount of effort and resources into the development of ultraviolet (UV) radiation sources that can be added to already existing processes related to the deposition and post deposition treatments of thin films. UV systems such as hollow cathode discharges [15, 16], constricted glow discharges [17], low pressure glow discharge from Hg lamps [18-22], and excimer lamps [15, 16, 23-35] have been used as additions to a variety of deposition techniques. Much research has been conducted with excimer lamps powered by radio frequency power supplies [23-29], but reports of microwave direct current magnetron power supplies have also been reported [36]. Radio frequency driven excimer based silent barrier discharge lamps have been the main contributors in a large part due to efforts by Boyd et al. Experiments include photo-induced deposition of silicon dielectrics such as silicon oxide, silicon nitride, and silicon oxynitride as well as direct oxidation of both Si and Ge substrates, and direct nitridation of Si surfaces [23, 24, 29]. High-k dielectric materials such as tantalum pentoxide (Ta_2O_5) have been deposited via a photo-assisted CVD process [26, 27] whereby absorbtion of the highly energetic photons emitted by the UV source results in the direct photodissociation of the precursor materials. Along similar lines, post deposition excimer UV annealing of the as-deposited samples has been conducted, compared, and thoroughly analyzed [26, 27]. Additionally, the decomposition of palladium acetate films for subsequent electrodeless deposition of metals [37, 38], surface modification of polymeric materials [39], and photo-assisted

conversion of polyamic acid to form low-k dielectric polymeric polyimide [40] have also been explored. The majority of this work was conducted using excimer lamps. However several early experiments were conducted with a low pressure glow discharge Hg lamp [41] that has served as a useful tool for comparison in more recent excimer studies.

Other groups have also investigated a variety of other UV radiation sources with respect to physical design and mechanisms for UV emission [15-17, 30-35]. Many of these are novel designs, but some are available from manufacturers (especially low pressure Hg lamps), and are discussed by the respective authors on a case by case basis. Deposition of silicon nitride on silicon by a low pressure Hg lamp [35], deposition of silicon nitride on III-V materials via a highly controlled photo-CVD process [19], and finally, the photolithic CVD of silicon dioxide utilizing an USHIO brand head on Xe excimer lamp [35] have also been pursued. Furthermore, Imai et al. [42] have looked into the densification of sol-gel films such as silicon dioxide and titanium dioxide by ultraviolet irradiation.

Silent Barrier Discharge Excimer Radiation

Since an in-house version of an excimer lamp was designed, built, and included in portions of the experimentation as an excimer UV radiation source, it is useful to look at a few of the properties associated with silent barrier discharges which seem to make this the best current option for a radiation source. First, with respect to other options available on the market, such as low pressure Hg lamps, the option of a Xe excimer lamp based on silent barrier discharge appears to be a superior option in several respects. The initial advantage lies in the power capabilities of the Xe lamp over the Hg lamp. Reported values for the Xe lamps range from as little as 10 mW/cm^2 to as great as 200 mW/cm^2 [24, 31, 35, 37, 43]. In comparison to low pressure Hg lamps, reported values

are less than 10 mW/cm^2 [28]. Intensities have been measured by a variety of methods, but commonly chemical actinometry or sodium salicylate scintillators coupled with monochromators have been used [28, 30, 36]. More recently, Ushio and Hamamatsu have made solid state photosensitive detectors for specific vacuum ultraviolet measurements.

The reason that such high intensities may be achieved has to do with the physics behind the generation of a silent barrier discharge. Using xenon as an example, the gas undergoes an excitation as a response to a radio frequency signal.

$$Xe + e \rightarrow Xe^* \tag{1-2}$$

$$Xe^* + Xe + Xe \rightarrow Xe_2^* \tag{1-3}$$

$$Xe_2^* \rightarrow Xe + Xe + h\nu(172nm) \tag{1-4}$$

The emission of radiation occurs in one of thousands of microdischarges that result as a function of radio frequency stimulus. As the sinusoidal oscillation of the voltage occurs, microdischarges may occur when a particular value for the voltage is achieved. This microdischarge remains until the change in voltage with respect to time is zero (i.e., dv/dt =0). This is shown graphically in Figure 1-5 [44].

Clearly, it is advantageous to have a higher flux of photons due to increased ability to dissociate various ambient gases (O_2), or precursor gases. Additionally, the greater photon flux may be advantageous with respect to the photonic effects, as the photons bombard the substrate and subsequently the growing film. The Xe excimer lamp has additional attractive features. First, the lamps are relatively inexpensive and easy to fabricate in comparison to other photo assisted processes where lasers or ion beams may be required [42]. The Xe lamp may also be easily adapted to very large areas by setting

up arrays of the lamps. This is particularly attractive for large scale applications in industry in the future if successful lab results support implementation. Additionally, the lamps are compatible with both atmospheric and vacuum operation. Xe excimers also exhibit narrow full with at half maximum (FWHM) values in single sharp emission spectra [23]. This is in contrast to the low pressure Hg lamps where a majority of the emitted radiation is actually occurring in a range above 200 nm which is above our range of interest. Both types of the emission spectra can be seen in Figure 1-6 [45]. To add to the low FWHM values, excimer lamps have a wide range of tunability with respect to the desired wavelength of radiation emitted. By simply changing the gas in the discharge region of the lamp, different wavelengths may easily be generated. This is illustrated in Table 1-2.

As mentioned previously, the lamp design that Boyd, in conjunction with Kogelschatz, has chosen to use has been developed based off of United States patent 4,837,484 dating back to 1989 [46]. In this patent, a fairly detailed description of an excimer lamp design based off of silent barrier discharge is described and several variations are presented. In this work, reference is also made to "prior art" in the Soviet journal *Zhurnal Prikladnoi Spektroskopii* in a publication entitled, "Vacuum-ultraviolet Lamps with a Barrier Discharge in Inert Gases." From these, we have also made an in house version of the lamp.

Materials and Properties

As identified in the literature, there are numerous options for high-k dielectric materials. Possibilities include tantalum pentoxide (Ta_2O_5), titanium oxide (TiO_2), cerium oxide (CeO_2), zirconium dioxide (ZrO_2), yttrium oxide (Y_2O_3), hafnium oxide

Table 1-2 Different wavelengths possible as a function of rare gas or rare gas halide mixture used for excimer decomposition.

Excimer Complex	Wavelength (nm)	UV Range
Ar	126	VUV
Kr_2*	146	
F_2*	158	
ArBr*	165	
Xe_2*	172	
ArCl*	175	
KrI*	190	
ArF*	193	
KrBr*	207	UV-C
KrCl*	222	
KrF8	248	
XeI*	253	
Cl_2*	259	
XeBr*	283	UV-B
Br*	289	
XeCl*	308	
I_2	342	UV-A
XeF*	351	

(HfO_2), aluminum oxide (Al_2O_3), and barium strontium titanate ($Ba_{0.5}Sr_{0.5}TiO_3$). As mentioned earlier, it is important to consider the main criteria associated with selecting a material. The main criteria that need to be taken into consideration for initial material consideration are permittivity, barrier height, and thermodynamic stability. As seen in Table 1-3, there are many options that are suitable for our investigation.

Ta_2O_5, TiO_2, and BST all lack a thermodynamic stability in direct contact with Si. This can immediately eliminate them from consideration as MOS candidates. However, BST will be investigated due to its extremely large permittivity and previous experiments that suggest it may be a feasible material in light of certain findings to be explained later. From the list of other remaining materials, it is only a matter of selecting materials that are predicted to fulfill the other criteria. Input from industrial sources and extensive research conducted on these materials suggest that Y_2O_3, ZrO_2, and HfO_2 are excellent

Table 1-3 Various properties of high-k oxide materials

Oxide Material	Dielectric Constant	Conduction Band Offset (eV)	Density (g/cm^3)	Melting Point (°C)	Stability in Contact with Silicon
Al_2O_3	9.3	2.8	3.97	2054	YES
$BaSr_{0.5}Ti_{0.5}O_3$	80 – 3600	-0.1 -0.1	6.02	1625	NO
CeO_2	7	---	7.65	2400	YES
HfO_2	~25	1.5	9.68	2774	YES
Ta_2O_5	24 – 65	0.3	8.20	1785	NO
TiO_2	80 – 170	---	4.23	1843	NO
Y_2O_3	10	2.3	5.03	2439	YES
ZrO_2	~25	1.4	5.68	2710	YES

candidates. These, along with BST, have been used for various portions of the studies.

Motivation

Intense activity in the microelectronics field to solve this problem is currently underway. Several different approaches including new innovative device architecture designs (e.g., vertical structures and double gate planar transistors [4]), alternative gate oxides, and new process integration have all been proposed to solve this problem. To date, new device architectures are still under development and not ready to be implemented into full scale production. The possibility of moving the deposition of the final gate dielectric to the post heat treatment portion of the CMOS process is a daunting task with respect to companies adding to the already existing infrastructures. The option whereby the gate dielectric is replaced with a new dielectric material of higher permittivity has been pursued by many research teams [8, 9, 47-49]. According to the equations that govern metal oxide semiconductor (MOS) technology, if a dielectric material with a higher dielectric constant were substituted for the current SiO_2 oxide, a thicker layer could be synthesized while still maintaining a capacitance per unit area that is equivalent to a very thin SiO_2 layer. This effect can be seen in the equation

$$t_{high-k} = \left(\frac{\kappa_{high-k}}{\kappa_{ox}} \right) t_{eq} \tag{1-5}$$

where t is thickness and κ is the dielectric constant of the respective high-k dielectric and the standard dielectric to be replaced. Another commonly referred to value is the equivalent oxide thickness (EOT) and signifies the thickness an equivalent SiO_2 layer would be if in fact the layer were SiO_2. This EOT value is paramount for research teams that desire to create a high-k gate stack that will be used in future MOS devices. This is because it is of no use to generate a layer that has an EOT thicker than if one were to just use SiO_2 in the first place. An additional equation that is easier to use to determine EOT when capacitance and gate area are known is

$$EOT = \frac{3.9 \times \varepsilon_O \times A}{C} \tag{1-6}$$

where 3.9 is the dielectric constant of a high quality SiO_2, ε_O is the permittivity of free space (8.854×10^{-12} F/m), A is the area of the gate, and C is the capacitance measured on the meter. This is simply a reorganized version of the more general equation for the capacitance of a MOS capacitor, where knowledge of any three of the four unknowns allows for calculation of the fourth

$$C = \frac{\varepsilon \varepsilon_O A}{t} \tag{1-7}$$

where all values are the same as above and ε is the dielectric constant of the high-k dielectric.

In theory, insertion of an alternative high-k dielectric layer is an attractive option, but in practice very difficult to achieve. The current SiO_2 dielectric layer for Si functions nearly ideally. Si is unreceptive to having that layer stripped and subsequent alternate

layers deposited in its place. There are problems with unwanted interfacial layers, which form during the deposition of the alternate dielectric layer, such as SiO_x, or silicates. The formation of an interfacial layer has the ability to quickly nullify any of the beneficial effects of an alternative high-k layer. This is so because it changes the equivalent electrical circuit that would describe the MOS capacitor from a single capacitor system to a double capacitor system. The new system has a capacitance associated with the high dielectric constant material in series with a capacitance associated with the low dielectric constant material. This is then expressed as an overall capacitance by the following equation:

$$\frac{1}{C_{Total}} = \frac{1}{C_{High-k}} + \frac{1}{C_{Low-k}} \tag{1-8}$$

Since the total capacitance is what would be the output on a measurement meter, a combination of this equation and equation 1-7 above, would allow for determination of the impact from each individual capacitance associated with both the high and low-k material. It should be easy to envision the desire to then apply these results a layer without any interfacial layer so that the total capacitance measured is 100% from the high-k layer with an end result of a much smaller EOT.

If it is possible to eliminate the interfacial layer, there are still problems associated with unacceptable defect levels in the oxide and at the oxide/semiconductor interface. This combination of issues has prohibited the generation of high enough quality layers for viable substitution.

In this research project, several of the more promising dielectric materials available have been selected and an attempt will be made to create a MOS capacitor with an alternate high-k material substituted in for the SiO_2. The objective of this research is not

to generate an alternate high-k MOS stack with an extraordinarily low EOT, but rather study the role that oxygen has with respect to the interfacial region. That is, if a low dielectric constant interfacial layer forms, what is its chemical nature, and if oxygen took part in the formation, what were possible sources for the oxygen. Additionally, high intensity ultraviolet radiation sources will be added (during deposition and post deposition processes) to investigate the role of ultraviolet radiation as it applies to changes it causes in dry oxygen systems. The radiation used in in-situ deposition processes is supplied by an array of low pressure mercury lamps, while post deposition annealing radiation is supplied by a xenon excimer ultraviolet radiation source. It will be shown that deep ultraviolet radiation has a definitive role during each of the processing steps and that it can be an effective way to alter device properties such as structural, chemical and electrical characteristics.

Oxygenation of Films

Numerous reports have claimed a direct connection of the leakage current of alternate high-k dielectric materials to the amount of oxygen vacancies associated with the grown film [50-53]. It is also well known that while pulsed laser deposition is an excellent technique for the stoichiometric transfer of materials to the growing surface, like many deposition techniques, there is typically also an oxygen deficiency associated with the films. Traditionally, these films have undergone post deposition O_2 treatments to help create more stoichiometric films and reduce the number of oxygen vacancies [54].

However, considerable effort has been placed on analyzing the effect of UV radiation as a method for creating more reactive oxygen species that will more effectively create stoichiometric structures and reduce oxygen vacancies. When radiation sources were added to conventional systems, photo-assisted growth of SiO_2 on silicon [20, 25, 29]

showed improvement with respect to enhanced oxidation rates and overall better properties, especially when the oxidations were conducted at temperatures much lower than those used in conventional dry oxidation. The addition of the low pressure Hg lamp to the system, which emits a majority of 254 nm radiation, but also a smaller percentage of 185 nm radiation [41], was claimed to have beneficial effects for the following reason. The radiation (especially the 185 nm portion) has the ability to convert normal dry oxygen (O_2) in the reaction vessels into more reactive gaseous species. The species generated include ozone (O_3) and other atomic oxygen species. This newly generated O_3 then undergoes a dissociation back to O_2 and atomic $O(^1D)$, ranging from several percent to greater than 10% in O_2 [41]. Boyd et al. claim that the atomic O has the ability to move more easily through the growing SiO_2 matrix which enables it to reach the Si interface more readily for enhanced growth rates. It will also combine with defects that occur during normal growth of SiO_2 resulting in better stoichiometric higher quality films.

According to later studies by Zhang et al, with photo-oxidation of silicon using a much higher intensity xenon excimer lamp, the O_2 in the system follows the following scheme. The bond energy of O_2 is known to be close to 5.1 eV and the energy, as calculated from the wavelength associated with Xe excimer emission, of the photons emitted from the xenon lamp are ~7.2 eV. This allows the following reaction to take place.

$$O_2 + h\nu(\lambda = 172 \text{ nm}) \rightarrow O(^3p) + O(^1D) \qquad (1\text{-}9)$$

The oxygen atoms released can subsequently form ozone by the following reaction

$$O_2 + O(^3p) + M \rightarrow O_3 + M \quad (M \text{ is a third body}) \qquad (1\text{-}10)$$

where M is a third body participant and can be either a buffer gas, or in many cases, just the oxygen that is already in the system. The ozone can then be decomposed by further absorption of the vacuum ultraviolet light or thermally, thereby producing additional excited state ^1D oxygen atoms:

$$O_3 + h\nu(\lambda = 172\ nm) \rightarrow O_2 + O(^1D) \quad (1\text{-}11)$$

The $O(^1D)$ atoms are claimed to be the main reason that enhancements are seen in samples that are processed with UV radiation due to their ease of moving about the matrices and/or their reactivity with defects inherent in the matrix. Additionally, the effect of the UV excimer radiation has also been adjusted as time progressed with respect to a second role of the UV radiation. This role is the effect of direct photonic bombardment of the surfaces from the energetic photons being emitted from the lamp. Wengenmair et al. [55] have shown in a study on TiN, where no oxygen is incorporated into the experiment, that UV radiation still caused differences in as-deposited samples versus UV deposited samples. This does serve as an indirect indication that photonic bombardment is playing a role in the UV process since no other process conditions were varied. Several different characterization techniques were used to confirm this observation.

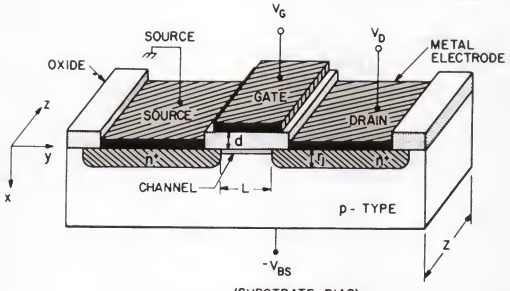

Figure 1-1 Schematic of a typical MOSFET [1]. The gate, insulator, and silicon form the metal oxide semiconductor capacitor portion of a MOSFET

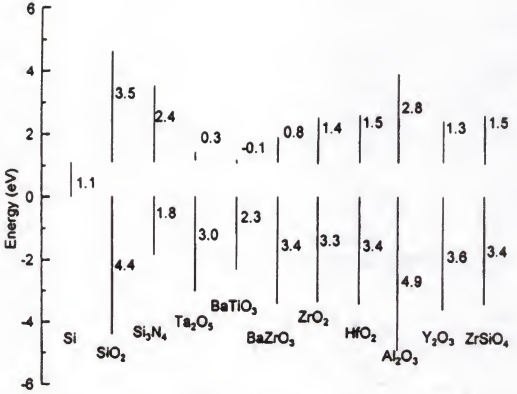

Figure 1-2 Calculated conduction and valence band offsets for various perspective alternative dielectric materials on Si [5].

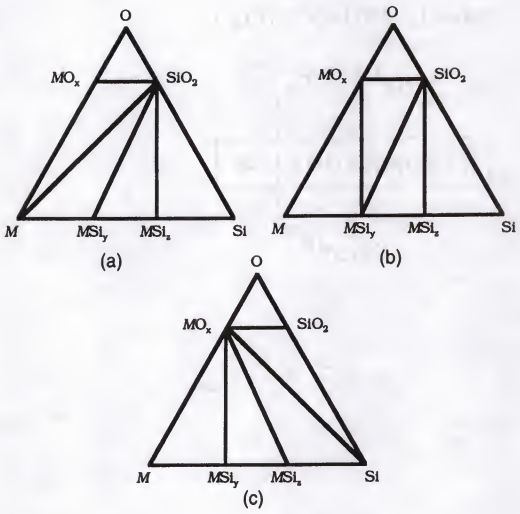

Figure 1-3 Ternary phase diagrams illustrating a) "SiO_2 dominant," b) "no phase dominant," and c) "metal oxide dominant" systems. System c represents a stable condition for a metal oxide when in direct contact with silicon [6]

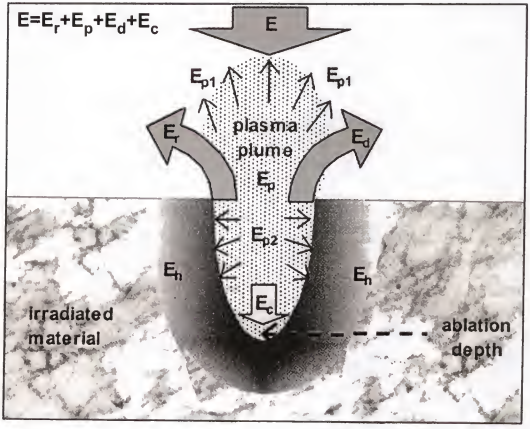

Figure 1-4 Schematic of total energy associated with laser ablation of a surface [15].

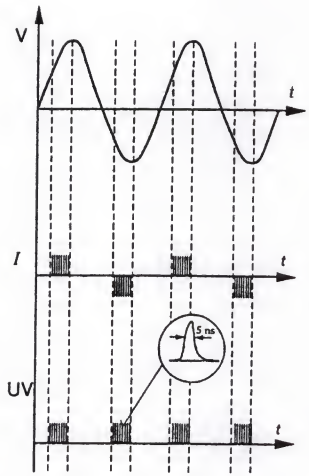

Figure 1-5 Sinusoidal voltage versus time plot indicating conditions where silent barrier microdischarges may occur [44].

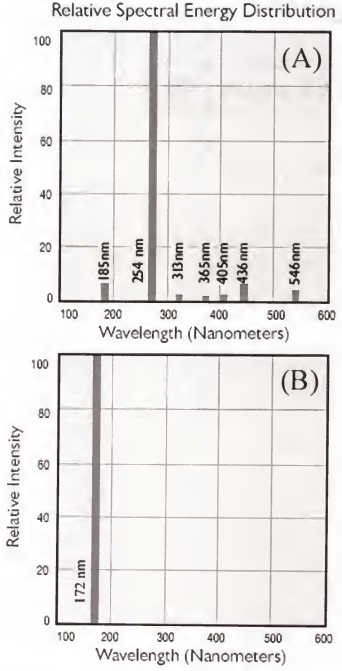

Figure 1-6 Spectral emission characteristics for A) low pressure mercury lamp and B) xenon excimer lamp. Plots adapted from [45]

CHAPTER 2
EXPERIMENTAL PROCEDURES

System Geometries

There are four main components used for experimentation. This includes the laser used for the laser ablation process, a traditional pulsed laser deposition (PLD) system that has been modified to an ultraviolet-assisted PLD (UVPLD) system and a homemade vacuum system equipped with a silent barrier discharge excimer lamp that is used for post deposition annealing of grown high-k dielectrics. The excimer lamp used for the post deposition system will be discussed in detail.

Laser System

A Lambda Physik LPX 305 i KrF excimer laser (s/n 9412 E 4188) was used for all laser ablation portions of the experimentation. This particular laser works in a pulsed mode delivering 25 nanosecond duration square wave shaped pulses at frequencies ranging from 1 – 50 Hz and output energies from 10 – 1100 mJ (fluence 0-3 J/cm^2). The computer is triggered by either an "internal" computer or from a remote "external" computer.

Excimer lasers work on the principle of stimulated emission of photons in a cavity where Kr, F, and a buffer gas are all contained. The Kr and F are elevated into excited states by application of very high voltages (16 -21 kV) so that excited KrF* complexes form and upon their decay give off single wavelength 248 nm radiation. As a result of specific cavity design, conditions exist whereby stimulated emission of coherent radiation

occurs and subsequent amplified high energy laser output in a pulsed mode can be obtained.

The laser radiation emitted from the cavity is directed through a series of lenses and an aperture until it finally impinges the sample. For the PLD system, the laser beam first traverses a collimation lens in an attempt to keep the radiation from diverging due to scattering as it passes through the ambient air. Immediately after the collimating lens, a 1 x 2 cm aperture is used to cut away the more diffuse lower energy edges from the incident beam. The beam then progresses into the chamber through an excimer grade fused silica window and then through a focusing optic with a focal length of 25 cm. Finally, a 2 mm thick quartz plate is used to protect the optic from material ablated from the target. Using a Gentec Sun Series EM1 energy meter (s/n 86052), the energy inside the chamber was determined after the pulsed laser beam had passed through all the optical components (without the focusing lens). An additional 10% of that was subtracted to take into account for the final focusing optic. From this value, divided by the area of the final spot size on the target, a precise calculation of the laser fluence was possible.

The ablation spot on the target had dimensions of 2 x 5 mm in a nearly perfect representation of the rectangular aperture used earlier in the beam path. This type of spot was achieved by adjusting the focusing lens position to a local greater than the focal point of 25 cm to a position ~35 cm, which coincided with the image plane of the lens. Because the aperture was used, imaging of it was possible and a spot with a highly uniform energy density was created. It was found that while ablation at the focal point resulted in a smaller spot size corresponding to a greater fluence, this was unnecessary

and detrimental to the setup. First, it was unnecessary because the threshold value for laser ablation of oxide materials frequently does not require high energy densities, as was the case in our experimentation. Second, taking the beam to the focal point resulted in a highly irregular spot geometry which also consisted of two additional satellite peaks to either side of the main ablation spot. The main spot was characterized by a Gaussian type energy distribution while the satellite peaks were clearly of a different energy all together. All samples grown in the PLD setup used this laser and optical setup.

UVPLD System

The pulsed laser deposition performed for this dissertation was done in a Neocera brand vacuum system. The entire system with laser, but without computer control is shown schematically in Figure 2-1. The system is a single chamber design that is routinely backfilled with nitrogen to atmospheric pressure so samples may be mounted and/or removed. It can easily reach vacuums of $1X10^{-6}$ Torr within an hour, $1X10^{-7}$ Torr within twenty four hours, and $1X10^{-8}$ Torr with the addition of liquid nitrogen cooling to the system. Vacuum is achieved via a Pfeiffer MD-4T oil free diaphragm roughing pump and a Pfeiffer TMU 230 turbo pump. A calibrated Neocera brand stainless steel resistive heater capable of 850°C is mounted vertically in the chamber and used to controllably heat and cool the substrate to and from the desired temperature. There is a computer controlled multitarget carousel available for depositions of up to six different materials for multilayer or superlattice experiments. An array of low pressure Hg lamps has been added to the conventional PLD setup to convert it into a UVPLD apparatus. Ultrapure gases may be added to the system through a highly sensitive Varian brand leak valve for a wide range of deposition ambients and pressures.

Excimer Annealing System

An in house vacuum system, seen in Figure 2-2, was setup for the purpose of post deposition annealing of samples. The system has the ability to reach high vacuum ($1X10^{-7}$ Torr) conditions via a Varian SD-450 two stage rotary vane roughing pump using Fomblin vacuum pump fluid coupled with a Pfeiffer TPU 170 turbo pump. There is precise atmospheric control via a highly sensitive Varian brand leak valve, and it is equipped with an Excel Instruments stainless steel resistive heater capable of up to 850 °C. The main feature of the system is an excimer lamp designed and built in-house that has been added to the system. The lamp was setup in a through mode so that the cylindrical quartz tubing of the lamp entered the vacuum chamber on one side through vacuum feedthroughs, traversed the entire vacuum cavity and exited another vacuum feedthrough out the other side. This is important in the design because it allows for efficient water cooling of the lamp as well as vacuum compatibility. The system is designed to accommodate full evacuation of essential portions of the excimer lamp ($1x10^{-6}$ Torr) and then, through a gas manifold, precisely backfill the lamp to any desired pressure up to atmospheric pressure with any gas of choice.

Excimer Lamp Design

The lamp design is based off of United States patent 4,837,484 (1989) and similar designs employed by Boyd et al. in London, England. The basic design of the lamp, as seen in Figure 2-3, entails the fusion of a pair of quartz tubes. The tubes are made from ultrahigh purity quartz (Suprasil) produced by Heraeus, and is the only quartz in the world capable of passing ~80% of the excimer ultraviolet radiation emitted by xenon complexes (172 nm). Standard high quality quartz will not pass any of the radiation at this wavelength. The quartz tubes are of two diameters so that one longer tube can fit

concentrically within the other, thus forming a gap. The ends of the shorter tube are fused to the longer tube in a way such that a constant gap along the length is maintained. An additional third tube (the gas inlet in Figure 2-3) must also be added to the tubes so that there is an access port to the gap. This tube will later be used as a port for pulling a high vacuum on the gap, and eventually for backfilling of any of a variety of gases capable of excimer decomposition. Table 1-2 shows a list of possible gases that may be used in a given lamp and the radiation wavelength they emit. The outer tube is then covered by a metallic mesh. The finer the mesh the better since there will be less obstruction for exiting radiation and therefore result in greater energy densities. This mesh is to be grounded. When mounted, the inside of the inner tube will serve two purposes. First, deionized water will flow through the system at all times during operation as an efficient cooling mechanism. As the power input into the system increases, the cooling water plays an increasing important role. Second, a metal wire capable of carrying high powers will be spiraled along the interior of the tube. This wire is connected to a radio frequency (RF) power supply (T & C Conversions, Inc.), that generates up to a 200 watt load to induce excimer decomposition. Figure 2-4 shows the microdischarges of the ignited excimer lamp located in the center vacuum portion of the high vacuum system.

Experimental Setups and Samples

There are three main areas that comprise the work discussed in this dissertation. As a result, it is important to delineate the various samples that were produced or modified in each stage, and discuss any preparations or modifications that were completed.

Interfacial Layer Formation

In this initial portion of the experimentation, the characteristics of an interfacial layer were investigated. Ultrathin ZrO_2 samples were deposited in a conventional PLD chamber and exposed to different ambient temperatures in a post deposition anneal. Vacuum, helium, and oxygen were used as annealing ambient gases. The main goal for this investigation was to try to determine the source or sources of oxygen that may exist during a typical deposition and, in particular, how they impact the characteristics of an unwanted interfacial layer. The conditions for deposition and post deposition heat treatments are shown in Table 2-1. The samples were investigated by variable angle spectroscopic ellipsometry, x-ray reflectivity, x-ray photoelectron spectroscopy, and Fourier transform infrared spectroscopy. These techniques will be discussed later in this chapter.

Table 2-1 Conditions for growth and post deposition heat treatments of thin ZrO_2 films

Sample	Post Deposition Anneal Atmosphere
1	No Anneal
2	Vacuum (6×10^{-6} Torr)
3	Helium (600 Torr)
4	Oxygen (600 Torr)

In-Situ Ultraviolet PLD

For this experimentation, a conventional PLD system has been fitted with an array of Hg lamps. The lamps emitted radiation in the ultraviolet and deep ultraviolet regions. That is, a majority of the radiation was emitted at ~256 nm, and a much smaller portion (~10%) at ~185 nm. The 185 nm radiation is responsible for the conversion of oxygen into ozone and other atomic oxygen species. Once the lamps were added to the system, Y_2O_3 and $Ba_{0.5}Sr_{0.5}TiO_3$ (BST) thin films were deposited. An optimum pressure of

ambient oxygen during ablation was determined for each of the materials. The optimization was done by comparing the full width at half maximum (FWHM) of a given x-ray diffraction peak of films deposited at different pressures. Table 2-2 shows the specific oxygen conditions used for the depositions.

Table 2-2 Conditions for in-situ ultraviolet annealing with an Hg lamp array during growth of BST and Y_2O_3 thin films.

	Oxygen Pressure (mTorr)	Ultraviolet Radiation
Barium Strontium Titanate		
1	20	NO
2	10	YES
Yttrium Oxide		
1	10	NO
2	4	YES

Once samples were obtained, they were characterized by variable angle spectroscopic ellipsometry, x-ray reflectivity, x-ray diffraction (glancing incidence x-ray diffraction), atomic force microscopy, transmission electron microscopy, current-voltage, capacitance voltage, and x-ray photoelectron spectroscopy.

Post Deposition Ultraviolet Annealing

In the final portion of experimentation, an array of hafnium dioxide (HfO_2) samples underwent a post-deposition excimer annealing step in the system shown in Figure 2-2. These films were deposited by a chemical vapor deposition technique by the Motorola Company on a 200mm p-type silicon wafer. The wafer was broken into smaller pieces and then placed in the excimer annealing chamber. The main difference with the excimer radiation compared to Hg ultraviolet radiation is that the emission in the ultraviolet region is a focused single sharp emission peak at 172 nm. Therefore, all of the radiation is acting to convert the dry oxygen into ozone and atomic oxygen. Table 2-3 shows the conditions for the post deposition anneals.

Table 2-3 Conditions for post deposition excimer anneals of HfO_2 thin films

	Anneal Temperature °C	Excimer Ultraviolet Radiation
1	No Anneal	-----
2	300	NO
3	300	YES
4	475	NO
5	475	YES
6	600	NO
7	600	YES

One set of samples was annealed in dry oxygen at temperatures of 300, 475, and 600°C. A second set of samples was grown in the presence of dry oxygen and excimer UV radiation, again at 300, 475, and 600°C. Both systems were at an oxygen pressure of 5 mTorr. An as-deposited control sample from the Motorola wafer that did not undergo any post deposition annealing was also analyzed. Upon annealing, the samples were tested by variable angel spectroscopic ellipsometry, x-ray reflectivity, x-ray diffraction (glancing incidence x-ray diffraction), atomic force microscopy, and capacitance voltage measurements.

Experimental Characterization Techniques

Several measurement techniques have been used to illuminate the differences seen between the samples that underwent radiation treatments versus those that did not. The properties of the films that were examined included structural, chemical, and electrical properties. Additional information is provided for the electrical characterization in the appendix due to its importance with respect to the ultimate goal of creating a better transistor.

Variable Angle Spectroscopic Ellipsometry

VASE is a very powerful, simple, and nondestructive means for determination of thickness in multilayered structures as well as optical properties such as index of

refraction and extinction coefficient. The optimum thickness range for ellipsometry is between 1-1000 nm and is well suited to the flat planar materials with low surface roughnesses generated for this dissertation. All measurements were made with a J. A. Woollam brand M-88 variable angle ellipsometer, with the angle of incidence set to 75°. This angle is optimum for semiconductor and microelectronic thin films. In this technique, the sample is subjected to a collimated beam of light from a xenon lamp. The light is adjusted so there is a known polarization state as is leaves the polarizer. After the beam of know polarization interacts with the sample, it will then exhibit a new polarization state. This new polarization state is interpreted by an analyzer, allowing a determination of the ratio of the complex Fresnel reflection coefficients and ultimately the psi and delta functions that are related to the properties of the sample. This method then requires the experimentally determined data to be compared to data from a theoretical model that is adjusted until a "best fit" can be found between the two. This does indicate that the better the theoretical model used for fitting, the closer the answer will be to the correct values. Since there is also the possibility that several different theoretical models fit well to one set of experimental data and may produce equivalently good fits, it is up to the user to evaluate and assimilate all information about the sample to develop a physically realistic theoretical model. It is therefore useful to make measurements at optimum wavelength and angle of incidence combinations to keep the assumed theoretical model simple yet realistic.

X-ray Reflectivity

X-ray reflectivity (XRR) measurements were made with the assistance of a Philips brand MRD X'Pert system. Data generated from an x-ray reflectivity plot include thickness, roughness, and density of a given material. Figure 2-5 is an example of a

typical plot showing how the different features of an acquired spectrum relate to the various data that can be extracted from the spectrum. Similar to VASE, the technique is well suited to smooth flat samples with low surface roughnesses and is most sensitive to samples in the 2-400 nm thickness range. This particular x-ray based analysis technique works by impinging the sample with x-rays over an array of angles ranging from slightly sub-critical angles to the first few degrees after the critical angle. The critical angle, also known as Brewster's angle, corresponds to the point at which x-rays change from total reflection off the surface to absorption and interaction with the sample as defined by Snell's law. The retrieved data results from monitoring the intensity of the x-ray beam reflected from various interfaces relative to the incident beam as a function of the scattering transfer vector. Fresnel equations will then describe the interaction of the x-rays with one another and with interfaces encountered in the structure. The constructive or destructive nature of the x-rays at a given angle results in generation of a fringe pattern. Similar to VASE, this pattern is compared to a user input model that incorporates thickness, roughness, density, and absorption parameters. Again, the better the input model, the more accurately the results will match the real physical structure.

X-ray Diffraction and Glancing Incidence X-ray Diffraction

XRD is most commonly used to identify crystalline phases and measure the structural properties of the phases such as strain, grain size, epitaxial quality, phase composition, preferred orientation, and defect structure. Additionally, the technique is noncontact and nondestructive and will produce spectra for films as little as 50Å in thickness. The basic setup of the diffraction process is seen in Figure 2-6. The premise of this relatively simple characterization tool is the generation of diffraction peaks due to constructive and destructive interference from x-rays scattered by the atomic planes in a crystal. The

condition for constructive interference from planes with a given spacing is given by Bragg's Law:

$$\lambda = 2d_{hkl}\sin\theta_{hkl} \quad (2\text{-}1)$$

where λ is the wavelength of the incident x-ray radiation (typically Cu Kα), d_{hkl} is the d-spacing between (hkl) planes, and θ_{hkl} is the angle between the atomic plane and the incidence direction for the x-rays. For single crystal films, there is only one specimen orientation that will satisfy the conditions for Bragg diffraction, however, with thin films that are polycrystalline, fiber textured, or exhibit preferred orientations, several families of planes may contribute to a diffraction system. X-ray diffraction data for this dissertation was obtained with a Philips MRD diffraction system. Once an x-ray diffraction pattern is generated, positive phase identification can be achieved by comparing measured d-spacing from the diffraction pattern (and their integrated intensities) to a known JCPDS powder diffraction standard.

In certain cases, it is not possible to get any type of diffraction pattern from a sample because the sample is either too thin or the peaks of interest are being masked by a much more intense peak that comes from the single crystal substrate. In this instance, a special mode of x-ray diffraction known as glancing incidence x-ray diffraction may be used. In this setup, the incident angle of the x-ray system is fixed at a small value (typically from 0.250-1.000°) and the receiving slit is allowed to scan through a typical range for a conventional XRD 2θ scan. As a result, only planes that satisfy the Bragg condition with the additional constraint in place will produce peaks. In a polycrystalline sample with many orientations, this will still generate a representative x-ray diffraction plot, but with much higher surface sensitivity and under proper conditions, without any masking peaks

from the silicon substrate. This method proved to be beneficial for several samples in this dissertation due to the low thicknesses used in different portions of the experimentation.

X-ray Photoelectron Spectroscopy

XPS spectra were collected using a Perkin Elmer 5100 installation using Mg Kα radiation at a takeoff angle of 90°. This technique is clearly one of the most broadly applicable general surface analysis techniques due to its high surface sensitivity and quantitative chemical state analysis capabilities. Elemental detection includes all elements except hydrogen and helium. Again, the smooth flat samples measured in this dissertation are optimum for this analysis technique. In the XPS process, high energy photons can ionize atoms to produce free electrons known as photoelectrons. The kinetic energy (KE) of the electron depends on the energy of the photon by Einstein's photoelectric law:

$$KE = h\upsilon - BE \qquad (2\text{-}2)$$

where $h\upsilon$ is the energy of the incident photon and BE is the binding energy. In this equation, $h\upsilon$ is known, KE is measured, and BE is therefore the determined output. The measured BE is specific to the atom concerned and thereby succinctly identifies the atom. Figure 2-7 shows the photoelectron process with carbon as an example. While the Mg Kα has sufficient energy (~1486.6 eV) to eject the innermost electrons from carbon, the photons may also remove the 2s or 2p electrons. XPS data may be interpreted by the user to give sensitive elemental and chemical state analysis.

Atomic Force Microscopy

Atomic force microscopy measurements were made with a Digital Instruments brand Nanoscope III operating in tapping mode. This technique was chosen for its exceptional

ability to produce topographic images of a surface in all three dimensions at remarkably high resolutions. If conditions are properly set, atomic resolution is attainable. This technique is also perfectly suited to the insulating, low roughness samples created for this dissertation. In an atomic force microscope, a sharp tip is mounted on a flexible cantilever. When the tip comes into close proximity of a sample surface, van der Waal forces repel the tip causing the cantilever to deflect. A piezoelectric scanner is responsible for moving the cantilever/tip assembly along the surface of the sample, while a laser reflecting off the end of the cantilever maps the topographical changes the cantilever senses. This is shown schematically in Figure 2-8.

Fourier Transform Infrared Spectroscopy

This method is one of the few techniques that provides information about the chemical bonding in a material, and is nondestructive. Here the goal is to determine changes in the intensity of a beam of infrared radiation as a function as a function of wavelength or frequency after it interacts with a sample. The FTIR used in these investigations is a Nicloet MAGNA 760 equipped with potassium bromide (KBr) optics and operating in transmission mode. The main feature is the ability to determine in a qualitative (and quantitative) sense the types of bonds that are present in a thin film structure.

Electrical Characterization

A primary tool for indication of quality of thin film is the use of electrical characterization techniques. After deposition or processing of thin films, metal oxide semiconductor (MOS) devices were fabricated and measured. Typical preparation of the film included the deposition of either gold (Au) or platinum (Pt) contacts via evaporation or DC magnetron sputtering, respectively. In both cases, a mask with an array of circular dots ranging from 25-500um was used to create dot arrays on the samples. The backside

contact was either evaporated Au or silver (Ag). In both cases, the backside of the wafer was cleaned and the surface was abraded so that clean silicon, without any native silicon dioxide, was present. It is of paramount importance to understand the consequences of which type of metal is chosen depending on what dielectric is deposited and whether the silicon substrate is n-type or p-type. If improper metals are chosen for a given setup, band alignment conditions may exist whereby non-ohmic contacts are created within the device itself. As an example, the backside metal contact on a p-type silicon wafer should have a work function greater than that of the silicon. If these conditions are met, there should be an ohmic contact, if not, the contact will be a rectifying Schottky contact. The most recent generation of a MOS capacitor fabricated for this dissertation is shown in Figure 2-9. After metallization of the front side contact (i.e., gate) was complete, samples underwent heat treatments either in an AG Associates rapid thermal annealing (RTA) furnace or in a conventional furnace. In both cases, in a forming gas atmosphere (10% H_2, balance N_2) was utilized. Both current-voltage and capacitance-voltage measurements were taken once the MOS capacitors were formed.

Current-Voltage Measurements

Once MOS devices were fabricated, a Keithley Instruments Inc., KI236 source measurement unit (SMU) was used to measure the current flow through a device. The 236 SMU was attached to a black box probe station equipped with a pair of Signatone Inc, micromanipulators. The micromanipulators were fitted with tungsten probes that were milled to produce a fine ~5 um tip. The output of the SMU was connected to the micromanipulator in contact with the gate (Pt or Au) while the input was connected to the backside contact (Ag or Au). This configuration is optimal for the determination of current leakage pathways directly below the device being measured (i.e., it avoids stray

leakage paths). Determination of the leakage current is an essential first step in analyzing an MOS device. Typically a current compliance threshold (a value that may not be exceeded) of 100 nA is input into the measurement parameters. Then a direct current bias sweep is conducted over a voltage range (usually negative to positive) and the amount of current that passes through the MOS structure is monitored. Typically it is best to start at a small voltage sweep range so that it is possible to determine if the device is leaky without causing a large amount of bias induced defects. The main goal of the leakage current measurement is to identify a high quality device that can be used for capacitance voltage measurements and to determine if excessive leakage is present that needs further investigation.

Capacitance-Voltage Measurement

Capacitance-voltage measurements serve as one of the most versatile and sensitive of all electrical characterization techniques. It is the ultimate tool for determining discreet differences in a MOS device that may serve as the final word in whether a given processing condition has resulted in a high enough quality device to apply to MOSFET applications. These measurements were carried out with a Kiethley Instruments Inc. Win-82 measurement system. This system, as seen in Figure 2-10 is comprised of four main components that work in unison. The Keithly 590 capacitance meter is used for high frequency capacitance measurements at 100 kHz and 1 MHz. The Keithley 595 capacitor is used for simultaneous quasistatic low frequency measurements. The Keithley 230 voltage source is used for static bias condition measurements. These three devices are wired into the Keithley 5951 remote input coupler, which serves to filter the device data to and from the various pieces of equipment. Due to its ability to give

detailed information about the quality of the MOS device, the Win-82 system will be discussed in the appendix.

The output of a typical CV curve can be seen in Figure 2-11. There are several important features that should be noted. First, there are three important regions with respect to gate bias voltage to take into consideration, known as accumulation, depletion, and inversion. The presence of the different regions is a result of the majority charge carriers (e.g., holes in a p-type silicon wafer) in the semiconductor. When a negative bias is applied to the gate electrode, positively charged holes are attracted from the semiconductor bulk region to the oxide/semiconductor interface where they accumulate (the accumulation region). The depletion region is generated when a gate is made less negative and the reduced field across the oxide allows the charge at the interface to diminish. As the sign on the voltage changes from a negative to a positive, majority carriers are repelled from the interface creating an area depleted of majority carriers (the depletion region). Finally, the inversion region is generated when the voltage becomes very positive and the depletion width has increased to a point where other mechanisms may become important. For example, in the depletion region, the product of the concentration of electrons and hole (np) is much less than the square of the intrinsic carrier concentration (n_i^2) and in this case, pair generation may occur and the subsequent minority carriers may migrate to the interface. The result of this is prevention of further depletion and a constant value for the capacitance. An additional possible scenario may occur whereby insufficient time is allowed for pair generation in which case a model called deep depletion will occur.

The high frequency measurement system has the ability to measure two different frequencies and using Metrics ICS software, two different equivalent circuit models, seen in Figure 2-12, to generate capacitance values. There are parallel and series models that represent two different physical structures. The series model addresses a capacitor in series with a resistance of some sort (possibly from the semiconductor). The equation that describes this scenario is

$$Z = R + iX \tag{2-3}$$

where Z is the impedance, R is the resistance, and X is the reactance. Additionally, the parallel model addresses a capacitor in parallel with some sort of conductance (possibly leakage through an ultrathin film). The equation that describes this scenario is

$$Y = G + iB \tag{2-4}$$

where Y is the admittance, G is the conductance, and B is susceptance. Note that the admittance, conductance, and susceptance are each the reciprocals of the impedance, resistance, and reactance, respectively. The reactance and susceptance can then be further described in a capacitive sense as:

$$\mathrm{X} = \frac{1}{\omega C_S} \tag{2-5}$$

$$Y = \omega C_P \tag{2-6}$$

where ω is the frequency of the setup and C_S and C_P are the capacitance when using the series model and parallel model respectively. The net impedance of the equivalent series and parallel circuits at a given frequency are equal, but the individual components are not:

$$R + iX = \frac{1}{G + iB} \tag{2-7}$$

If there is a lossless circuit (i.e. $R = 0$ and $G = 0$) the C_S and C_P are equal. However, since circuits do have losses, a dissipation factor is added to the system.

$$D = \omega C_S R \tag{2-8}$$

$$D = \frac{G}{\omega C_P} \tag{2-9}$$

Through further numerical manipulation, it is determined that conversion from one equivalent circuit model to the other is readily possible as seen in Table 2-4

Table 2-4 Conversion factors for series-parallel electrical equivalent circuits.

Model	Dissipation Factor	Capacitance	Resistance or Conductance
Parallel C_P, G	$D = \frac{1}{Q} = \frac{G}{\omega C_P}$	$C_s = (1 + D^2)C_P$	$R = \frac{D^2}{(1 + D^2)G}$
Series C_S, R	$D = \frac{1}{Q} = \omega C_S R$	$C_P = \frac{C_S}{1 + D^2}$	$G = \frac{D^2}{(1 + D^2)R}$

This treatment has been applied to illustrate how capacitance values are generated from the impedance values and subsequent conversion to series and parallel cases. As mentioned earlier, the series represents a physical scenario where a capacitor is in line with some type of resistance, while the parallel mode represents a physical scenario where a capacitor is in parallel with some type of conductance. This however does not take into consideration the physical possibility of an ultrathin film that is leaky, but also encounters resistance from the substrate. In this case, a three element electrical circuit, also seen in Figure 2-12, could be analyzed in a similar manner as above to develop equations for converting from either the parallel or series mode to the three element equivalent circuit that more appropriately represents the physical structure.

Transmission Electron Microscopy

The TEM microscope has among the highest lateral spatial resolution in imaging mode of any characterization technique. The TEM used for analysis is a Jeol 2010 high resolution microscope with a nominal spatial resolution of 1.8Å. Additional features of the microscope include diffraction information, energy dispersive spectroscopy, and electron energy loss spectroscopy. The fundamental basis for the TEM is generation of an electron beam from an electron gun. The electron beam then passes through a variety of lenses and impinges an ultrathin sample. As seen in Figure 2-13, both scattered and unscattered electrons that penetrate the sample thickness comprise the TEM signal. Sample requirements for TEM analysis are quite stringent in the sense that they must be less than 200nm thick. For the analysis done here, samples were made so that cross sectional analysis was capable. Though this type of sample preparation is much more complex and delicate than conventional sample preparation, this type of measurement gives the ability to determine the thickness of a grown film, which can then be input into VASE and XRR models to help develop more realistic and truly physical models.

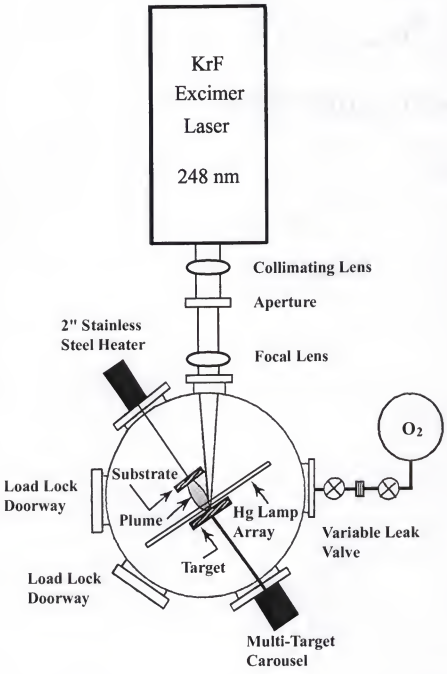

Figure 2-1 Ultraviolet-assisted pulsed laser deposition system, KrF excimer laser, and optic setup.

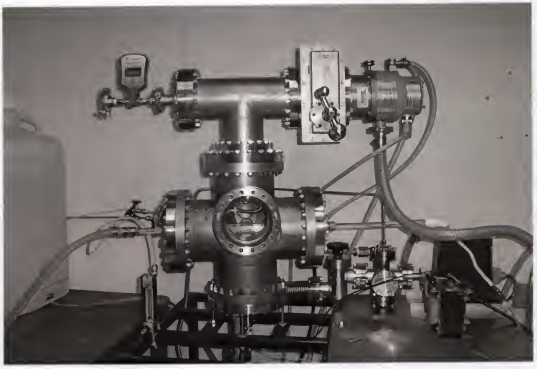

Figure 2-2 Homemade excimer annealing system equipped with vacuum ultraviolet lamp.

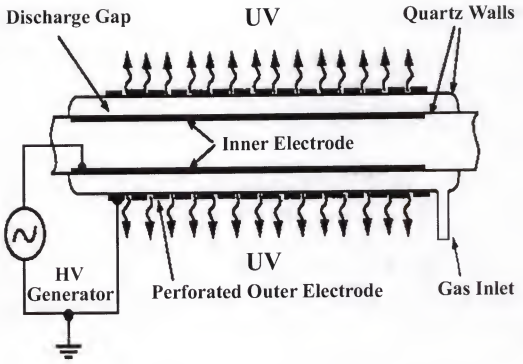

Figure 2-3 Schematic of excimer lamp illustrating the concentric tube design and how a radio frequency load is delivered to the system. Figure adapted from [44].

Figure 2-4 Tiny microdischarges from the ignited excimer lamp are the origin of the excimer radiation.

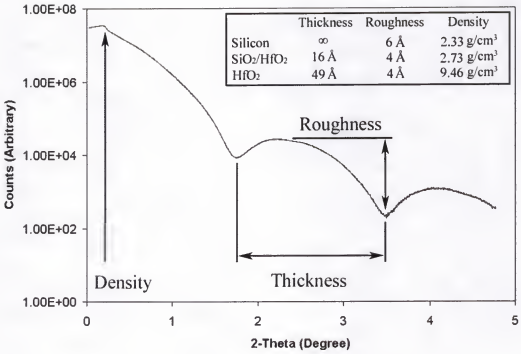

Figure 2-5 General x-ray reflectivity setup showing physical relationships between the acquired data and the modeling output.

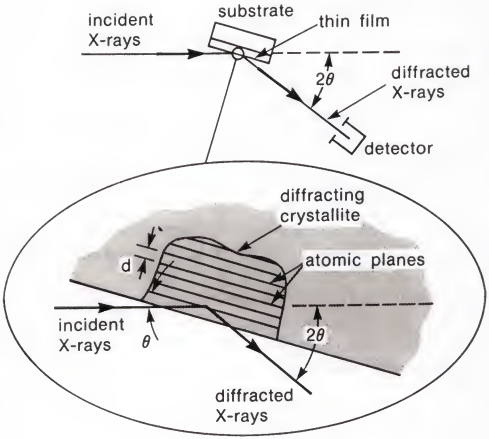

Figure 2-6 General x-ray diffraction setup illustrating the interaction of x-rays with a structure as they pertain to Braggs Law [56].

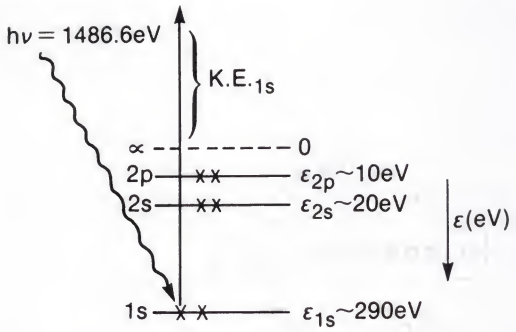

Figure 2-7 Process of incoming radiation ejecting a characteristic photoelectron from a carbon sample [56]

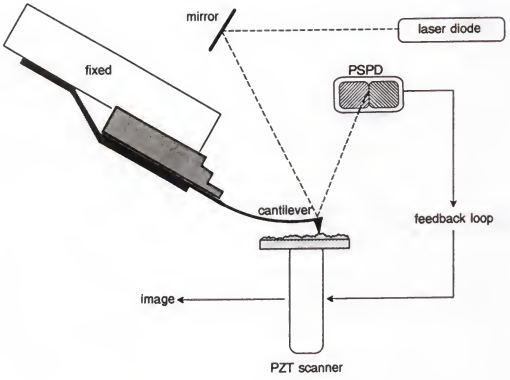

Figure 2-8 Schematic of atomic force microscope and the various components that allow up to atomic resolution [56].

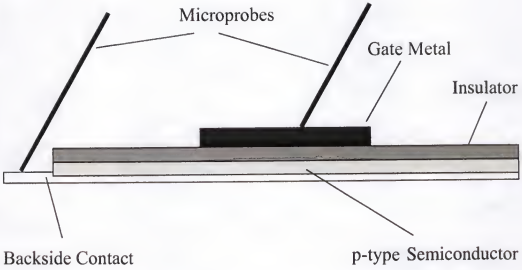

Figure 2-9 Typical MOS capacitor prepared for this dissertation.

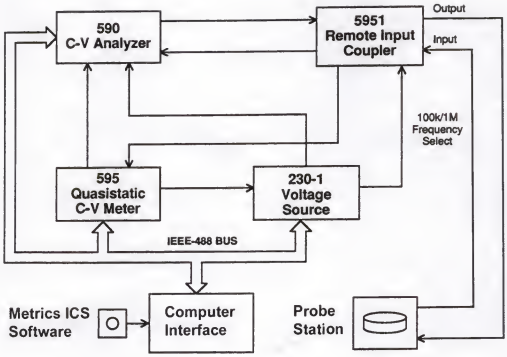

Figure 2-10 Block diagram of Keithley Win-82 system and how it connects to the probe station. Adapted from Keithley Win-82 operation manual.

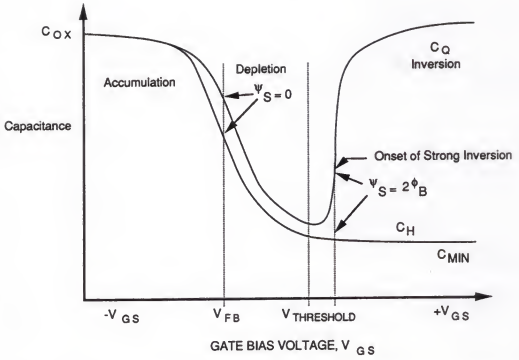

Figure 2-11 Typical capacitance-voltage illustrating the three main regions that occur in a MOS device as a function of bias voltage applied. Adapted from the Keithley Win-82 operation manual.

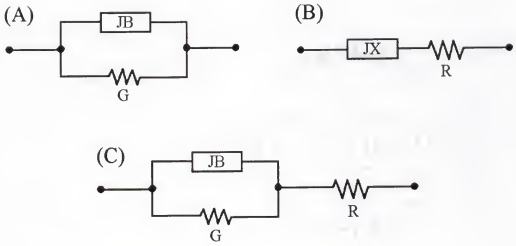

Figure 2-12 A) parallel, B) series, and C) combined series and parallel models for generation of capacitance information.

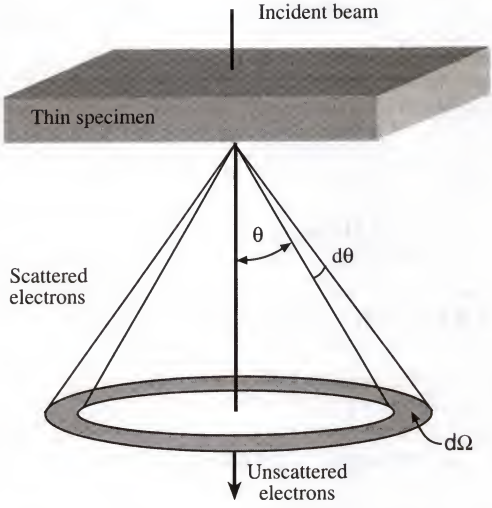

Figure 2-13 Schematic of electron beam after passing through an ultrathin TEM sample. Some electrons are scattered while others remain unscattered [56].

CHAPTER 3
INTERFACIAL LAYER FORMATION

As mentioned previously, many research teams have been searching for an alternative high-k dielectric material to replace the currently used SiO_2. Although this procedure appears to be simple, implementation of this new layer has encountered problems. One such problem is the presence of an unwanted interfacial layer that forms between the silicon substrate and the alternative high-k dielectric layer. The composition of the interfacial layer was and still is a topic of considerable debate with respect to its origin and composition. Though it is commonly accepted that oxygen plays an intricate role, the exact modes are not well understood. This portion of experimentation looks into these questions as they pertain to oxygen conditions in the pulsed laser deposition (PLD) system during post deposition heat treatments.

Anneal Conditions

For this study, four identical ultrathin ZrO_2 samples were grown by conventional PLD and then subjected to high temperature anneals in different ambient gases without breaking vacuum conditions in the deposition chamber. Due to analysis requirements, a special mount was used to attach the silicon by mechanical contact only to the substrate heater. This was in contrast to the typical method of attaching the samples with silver paste. Because of the alternative mounting technique, there was an increase in thermal losses associated with the substrate so even though the substrate heater is capable of 850°C, annealing temperatures were limited to 750 °C. Of the four samples, the first sample was not heat treated in any way so that comparison of an as-deposited sample

could be conducted. The remaining three samples were annealed for 10 minute increments in vacuum, ultra high purity (UHP, 99.999995%) helium, and UHP oxygen. Table 3-1 shows the respective partial pressures of oxygen for the various low, mid, and high conditions.

Table 3-1: Partial pressure of oxygen for respective deposition ambients.

Sample	Actual Pressure (Torr)	Oxygen Partial Pressure (Torr)
As-deposited	--	--
Vacuum annealed	$5x10^{-6}$	$5x10^{-10}$
Helium annealed	600	$6x10^{-4}$
Oxygen annealed	600	600

Once the samples were processed, they were analyzed by variable angle spectroscopic ellipsometry (VASE), x-ray reflectivity (XRR), Fourier transform infrared spectroscopy (FTIR), and x-ray photoelectron spectroscopy (XPS). Additionally, a cross sectional transmission electron microscopy (XTEM) investigation of the oxygen annealed sample was performed.

A 239Å SiO_2 on silicon calibration wafer was used before any data was collected to verify the accuracy of the VASE probe station. When the samples were measured, a model with ZrO_2 on silicon was used. Additional models with an additional interfacial layer was considered, however, it was found that more detailed models would return to a single layer model when the fitting iterations were allowed to proceed. From the four samples, the following data shown in Table 3-2 was collected by VASE.

There is an increase in overall thickness of the sample as the amount of oxygen in the system increases. Since all of the samples were grown under identical conditions, the

Table 3-2: VASE thickness measurements of ZrO_2 samples after post-deposition heat treatments in various ambients.

Sample	Thickness (Å)
As-deposited	39
Vacuum annealed	43
Helium annealed	47
Oxygen annealed	48

thickness of the ZrO_2 layer is not expected to increase. However, the overall thickness may increase if there is an additional second layer that cannot be individually discerned by the ellipsometer, but does exist and adds to the overall thickness.

XRR analysis of the four samples was completed. The data from the VASE measurements were used as starting thicknesses for modeling of the XRR spectra. Since XRR data takes thickness, roughness, and density of any number of layers into consideration, it is of utmost importance to have an approximate idea of the model as it pertains to the actual physical sample. As an example of the importance of a good model to describe the experimentally acquired data, the oxygen annealed sample is shown in Figure 3-1 with a variety of modeling options.

Figure 3-1 shows the acquired "Raw Data" XRR scan and three different modeling possibilities. The first modeling possibility labeled, "1 Layer Model Without Fit" represents the situation where the user input values for thickness, roughness, and density for a single layer of ZrO_2 on top of single crystalline silicon (This would represent the ideal case). After inputting the data, no additional processing was conducted. A value known as the mean square error (MSE) serves as an indication of the quality of fit between the model and the experimental data. The MSE value for the "1 Layer Model Without Fit" was $\sim 1x10^2$. As a reference, a poor MSE would be $\sim 1x10^2$ whereas an excellent fit would be around $1x10^{-3}$. The next modeling possibility labeled, "1 Layer

Model With Fit" is identical to the previous model, however, additional processing step is allowed to occur. The additional processing is an iterative modeling sequence where the initial values input from the user are allowed to vary in an attempt to develop a better fit (i.e., a lower MSE value). The iterative sequence must be carefully monitored because it is possible to obtain a mathematically lower MSE value by losing the physical reality of the model. For this example, the density of the ZrO_2 layer has veered from the ideal value of 5.68 g/cm^3 and become a physically unrealistic value of 4.77 g/cm^3. The MSE associated with this second model was ~$1x10^{-1}$. The final model labeled, "2 Layer Model With Fit" shows that with the addition of a second layer between the ZrO_2 and the silicon has a profound positive effect by generating a realistic model exhibiting a very low MSE value of $8x10^{-3}$. The data for the three different models are shown in Table 3-3.

Table 3-3: Thickness, roughness, and density data for the various XRR model options for the oxygen annealed ZrO_2.

1 Layer Model Without Fit	Thickness (Å)	Roughness (Å)	Density (g/cm^3)
Silicon Substrate	∞	5	2.33
ZrO_2 Layer	48	4	5.68
1 Layer Model With Fit			
Silicon Substrate	∞	8	2.33
ZrO_2 Layer	45	2	4.77
2 Layer Model With Fit			
Silicon Substrate	∞	4	2.33
Interfacial Layer	22	6	2.40
ZrO_2 Layer	16	4	5.88

With respect to the two layer model, initially a density for a pure amorphous SiO_2 (2.19 g/cm^3) [57] layer was input, but this proved inadequate to perfectly describe the

desired data until the density of the interfacial layer was allowed to vary. Upon variation, the density increased to a value of 2.40 g/cm^3 and allowed for the very low MSE value shown above. The impact of the higher density value will be discussed later and it will be explained why this is still an acceptable physically realistic value.

Since the importance of the "2 Layer Model With Fit" has been shown, all future XRR analysis will implement this type of model. Figure 3-2 shows the four XRR spectra corresponding to the as-deposited, vacuum, helium, and oxygen annealed samples and the modeling associated with each. The modeled values are shown in Table 3-4.

Table 3-4: Modeling data for the as-deposited, vacuum, helium, and oxygen annealed samples.

As-deposited	Thickness (Å)	Roughness (Å)	Density (g/cm^3)
Silicon Substrate	∞	4	2.33
Interfacial Layer	12	4	2.68
ZrO_2	21	5	5.86
Vacuum Anneal			
Silicon Substrate	∞	5	2.33
Interfacial Layer	14	3	2.67
ZrO_2	21	5	5.86
Helium Anneal			
Silicon Substrate	∞	3	2.33
Interfacial Layer	17	4	2.58
ZrO_2	20	5	5.63
Oxygen Anneal			
Silicon Substrate	∞	4	2.33
Interfacial Layer	22	6	2.4
ZrO_2	16	4	5.88

Figure 3-2 shows that the two layer model was effective in interpreting all of the different anneal conditions. From Table 3-4, there are two important features that should be noted with respect to the interfacial layer. First, the interfacial layer is the thinnest for

the as-deposited sample at 12 Å and increases to 14, 17, and 22 Å when annealed in vacuum, helium, and oxygen, respectively. Second, a similar trend is seen for the densities of the interfacial layer. In this situation, the density is greatest for the as-deposited sample at 2.68 g/cm^3 and decreases to 2.67, 2.58, and 2.40 g/cm^3 when annealed in vacuum, helium, and oxygen respectively. Figure 3-3 shows how as the partial pressure of oxygen in the system increased, the density of the interfacial layer decreased.

Since XRR investigations indicated that an interfacial layer was present, an XTEM sample was prepared from the oxygen annealed sample. This was to determine if the micrograph would support the interfacial layer data exhibited in the XRR. As shown in Figure 3-4, it is clear that the sample is composed of two distinct layers atop the single crystal silicon. Unlike the ideal structure that would exhibit a single ZrO_2 layer atop the silicon, there is a distinct polycrystalline ZrO_2 layer atop an amorphous layer atop the single crystalline silicon substrate. From the micrograph the thickness of the polycrystalline layer is ~20Å and the thickness of the amorphous layer is also ~20Å.

The next step in the investigation led to measurement of the samples by FTIR with a Nicolet MAGNA 760 instrument in transmission mode. In this case, the backside of the samples was cleaned and underwent a 1% hydrofluoric (HF) acid cleansing immediately prior to their placement into the nitrogen purged FTIR bench chamber. By using HF on the backside of the samples immediately prior to their measurement, this ensured that any signal response from the infrared measurement would be not be attributed to Si—O bonds on the backside of the oxidized silicon sample and could only originate from the dielectric side of the sample (i.e., the interfacial region). Figure 3-5 is a compilation of

the results recorded from the as-deposited, helium, and oxygen annealed samples. Inspection of the plot reveals that the as-deposited control sample already showed a peak located around 1080 cm^{-1} relating to Si—O—Si bonding in stretching mode. Upon annealing in helium, the area under the 1080 cm^{-1} peak increased by ~93%. When annealed in oxygen, the area under the peak increased by ~190% with respect to the as-deposited peak. Peaks at 800 and 460 cm^{-1} corresponding to Si—O—Si bending and rocking modes also showed similar increases in absorption. [58, 59]

The next step in the analysis process included a detailed investigation of the various XPS peaks. Figure 3-6 shows the Si 2p peaks as acquired at a take-off angle of 90° without any sputtering for the different annealing conditions. There are two prominent peaks associated with the Si 2p region. There is one peak that is located at ~99.3 eV which is attributed to the silicon substrate and a second peak that located at ~103.3eV which is attributed to silicon bonded to oxygen in the interfacial layer. While the position of the peak located at ~99.3 eV remains relatively constant, the position of the higher binding energy peak is continually changing as a function of annealing condition. For the as-deposited sample the higher energy peak is located at ~103.1 eV. Annealing in vacuum, helium, and oxygen resulted in a continual increase to values of 103.2, 103.3, and 103.5 eV, respectively. The vertical line located at ~103.6 eV seen in Figure 3-7 corresponds to silicon bonded to oxygen in a pure thick SiO_2 layer. [60]

Analysis of the XPS O 1s peaks reveals a single peak exhibiting an asymmetric shape indicative of multiple chemical species. In order to analyze this type of peak, a fitting program is utilized whereby the single asymmetric peak is deconvoluted into two or more Gaussian peaks. An example of the fitting process can be seen in Figure 3-8 which

shows A) the raw data peak, B) 1 peak fit, C) 2 peak fit, and D) 3 peak fits. Similar to the XRR fitting program, the XPS fitting program also has an MSE value that it generates as a quality of fit for the different types of models. From Figure 3-8, for the oxygen annealed sample, it is clear that a single peak fit is totally unacceptable as well as exhibiting an unacceptably large MSE value of 28.5. As seen in B, the two Gaussian peak fit has a much better MSE value of 6.5, but is still not considered a good fit. This is because the full width at half maximum (FWHM) associated with the peak reaches a value of 2.25 eV. Typical values for a peak representing this type of layer will be more in the 1.5 eV range. This leads to the three peak fit shown in C that has a good MSE value of 4.8. Additionally, each of the peaks exhibit reasonable values for FWHM and can be accounted for in a physical manner. For this example, peak A is corresponded to oxygen bound to zirconium, peak B corresponded to oxygen bound to silicon, and peak C is associated with trapped physisorbed oxygen present in the pulsed laser deposited films. Not all XPS peaks call for three peaks to obtain a good fit. The key it to always have a physical model that explains the fit well and also remains within reasonable boundary conditions.

Figure 3-9 shows the three peak fit for each of the four anneal conditions. Peaks are located at A) ~530.2, B) ~531.5, and C) ~532.0 eV corresponding to oxygen bound to zirconium, silicon, and physisorbed oxygen, respectively. The binding energy of the oxygen bonded to zirconium O 1s peak matches perfectly with its standard location of ~530.2 eV in all annealing conditions while the binding energy of the oxygen bonded to silicon O 1s peak is ~1 eV lower than its pure bulk SiO_2 value of ~532.5 eV [60]. As with the trend seen in the Si 2p peaks, Figure 3-10 shows a similar trend also occurs with

the binding energies of the oxygen bonded to silicon O 1s peak. Again, a continuous shift that corresponds directly to the amount of oxygen in the system changes the binding energies to values farthest from pure SiO_2 in low oxygen conditions and nearest to pure SiO_2 in high oxygen conditions. In addition to the shifting of the peak, there is an additional change to note. This second change relates to the size of peak C corresponding to trapped oxygen in the film. Analysis of oxygen content reveals that the amount of oxygen trapped in the film corresponds to ~15% for the as deposited film while all of the annealed films reduced to a value of ~10%. This important result shows a decrease of 5% of the trapped oxygen in the film structure when annealed.

Interpretation of the data reveals several important results from this study. First, VASE measurements were conducted as an initial measure of the thickness of the sample. While the VASE system was unable to discern discreet differences in the layer, it was able to detect an increase of the overall layer thickness. Since the ZrO_2 would not be expected to increase during a post deposition anneal, this seemed to indicate growth of a second non-ZrO_2 layer. The data from the VASE was used as a first approximation in the XRR modeling where the fit revealed that a single ZrO_2 layer atop a silicon substrate model was insufficient to describe the shape of the experimentally acquired data. As a result, an additional layer was added between the ZrO_2 and the silicon substrate as an interfacial layer. The interfacial layer was initially given a density of pure amorphous SiO_2 (2.19 g/cm^3) [57] which represented the theoretical scenario where the interfacial layer is composed entirely of SiO_2 and no other species or compounds are present. Without any fitting procedures, this was still an improvement over the single layer model, but by allowing the density of the interfacial layer to vary, excellent fits with very low

MSE values were obtainable for the as-deposited sample and all of the annealed samples. The important ramification of the density variations was that the density of the interfacial layer was always larger than that of pure amorphous silicon. The values began at a value of 2.68 g/cm^3 and decreased toward a more SiO_2 like density as anneal conditions incorporated more oxygen. The sample annealed in pure oxygen exhibited an interfacial layer of 2.40 g/cm^3. This important result indicates that the structure of the interfacial layer is not a pure SiO_2, but instead may include higher density materials such as Zr metal in a silicate-like structure, or ZrO_2 in a physical mixture with SiO_2. Other options include a layer that consist of a pure SiO_2, silicate, or silicide, but this cannot be the case, since the density of these layers are 2.19, 4.6, and 4.88 g/cm^3, respectively [57]. As an additional confirmation of the existence of the interfacial layer, an XTEM micrograph was prepared. Indeed, for the oxygen sample, an amorphous interfacial layer ~20 Å in thickness and a polycrystalline layer of ~20 Å was observable. This result correlated well with the XRR results. The FTIR conducted on the samples revealed a substantial increase in area under the 1080 cm^{-1} peak (Si—O—Si stretching mode) when the helium anneal was conducted and an even larger increase when the oxygen anneal was conducted. This increase in absorbance indicates physically more Si—O bonding associated with the structure and agrees well with the density and thickness variations seen in the XRR data. That is, as the oxygen content in the anneal conditions increase, the density of the interfacial layer became more like SiO_2. XPS investigations of the Si 2p and O 1s regions further supported the existence of the interfacial layer and more importantly that it was not composed of a pure SiO_2. The fact that the Si 2p located around ~103 eV (instead of 103.6 eV for pure SiO_2) shifts to higher binding energies as a

function of oxygen content indicates that there is either a more complex bonding environment for the silicon bonded to oxygen, or a thin film artifact. XRR and FTIR data both indicate that a more complex bonding environment more aptly explain this discrepancy. Oxygen diffusing to the interface and reacting to form SiO_2 explains the change in density seen by the XRR scans and the increase in Si—O bonds exhibited by the FTIR spectra. The O 1s peak associated with oxygen bonded to silicon is ~1 eV away from its pure bulk SiO_2 value of ~532.5 eV [60]. Similar to the Si 2p peaks, the binding energies of the oxygen bonded to silicon continuously shift from values farthest from pure SiO_2 at low oxygen conditions to values nearest SiO_2 for the pure oxygen annealed sample.

All of the proceeding data question the source of the oxygen species that make up the interfacial layer and the composition of the interfacial layer. The oxygen may come from the ambient gases that are used during the heat treatments [61], from trapped oxygen located within the grown ZrO_2 film [62-64], or from direct chemical reaction between the silicon and the grown layer [65].

Due to the predicted thermodynamic stability of ZrO_2 in direct contact with silicon at 1000 °C [6], a chemical reaction between the grown ZrO_2 film and the silicon substrate is unlikely. XPS data supports the migration of trapped oxygen in the ZrO_2 film under high temperature treatments. The O1s peak located at ~532 eV and corresponding to trapped oxygen is seen to decrease from a concentration of ~15% in the as-deposited control sample to values in the 8 – 10% range for samples that underwent anneals. Growth of the interfacial layer during deposition has previously been connected to the amount of trapped (physisorbed) oxygen present in the films [64]. However, the amount of oxygen

that is available in the trapped state is limited. The significant growth of the interfacial layer requires an additional oxygen source. The source is oxygen from the ambient diffusing through the grown sample, migrating to the interface, and reacting within the interfacial region. This is easily an acceptable notion since crystalline ZrO_2 is a relatively open structure that is a good oxygen conductor.

Ultrathin ZrO_2 films were deposited on silicon and then heat treated in different atmospheres representing different oxygen conditions. VASE, XRR, XTEM, FTIR, and XPS were utilized to determine A) if an interfacial layer was present and B) if there was, what role oxygen played in the origin and composition of the layer. It was found that the various characterization tools did indeed support the existence of an interfacial, even for the as-deposited sample. The composition was determined to be a physical mixture of ZrO_2 and SiO_2 that could be affected by oxygen in the system. It was also determined that oxygen in the system originated from two sources. The first of these was trapped oxygen in the film and the second was from diffusion of ambient gases through the film to the interfacial region. Due to these two mechanisms, it has been concluded that it would be very difficult to achieve an oxide based alternative high-k dielectric on silicon without forming an interfacial layer by conventional PLD.

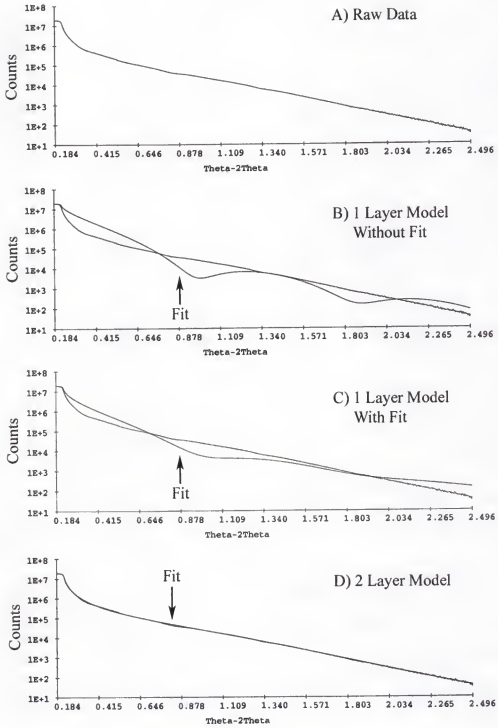

Figure 3-1 XRR spectra of A) raw data, B) 1 layer model without fit, C) 1 layer model with fit, and D) 2 layer model with fit illustrating the importance of a good model when analyzing XRR data.

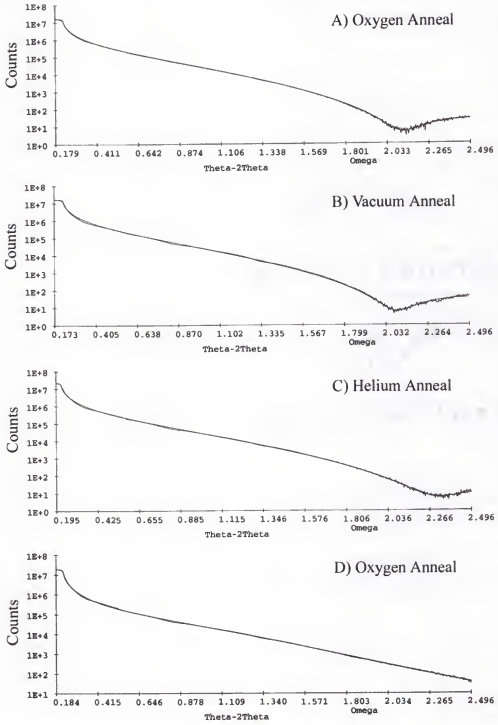

Figure 3-2 XRR spectra of A) as-deposited, B) vacuum annealed, C) helium annealed, and D) oxygen annealed ZrO_2 thin films as modeled with the "2 layer model with fit".

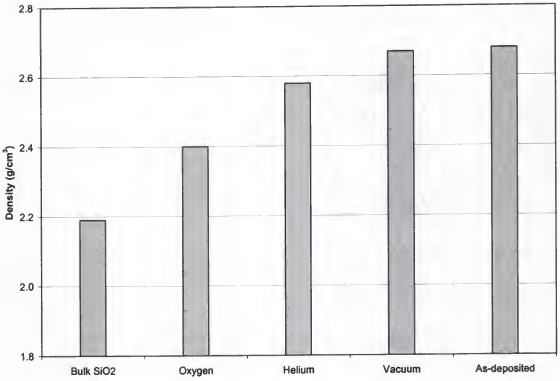

Figure 3-3 Plot of interfacial layer density as determined by XRR as a function of oxygen content in the annealing system. Bulk SiO_2 has been added as a reference.

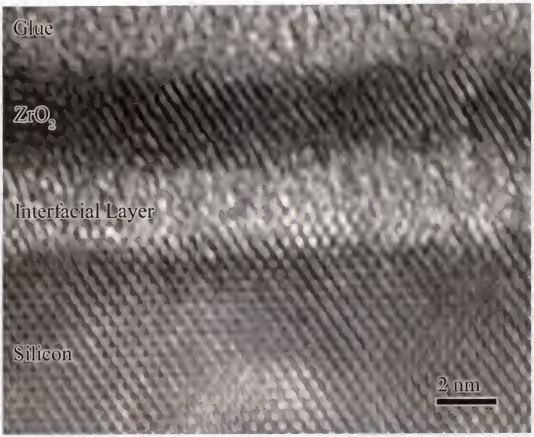

Figure 3-4 Cross sectional TEM of a polycrystalline ZrO_2 thin film atop an amorphous interfacial layer atop single crystalline silicon.

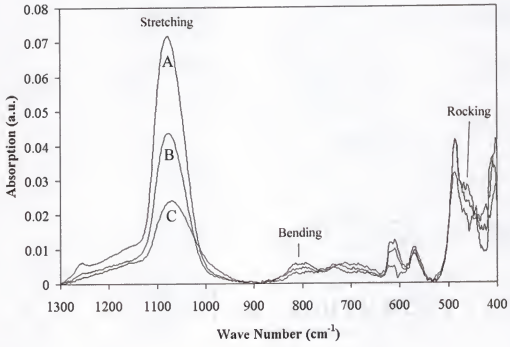

Figure 3-5 FTIR spectra of A) oxygen anneal, B) helium anneal, and C) as-deposited ZrO_2 thin films showing the increase in Si—O bonding absorption in stretching, bending and rocking modes.

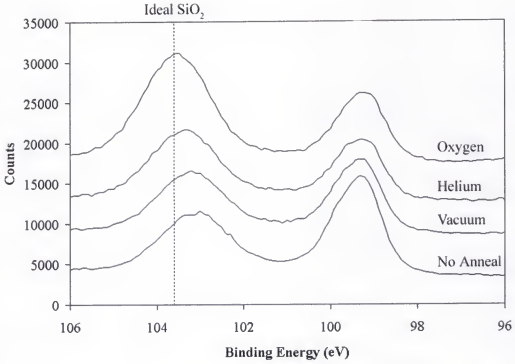

Figure 3-6 XPS data of Si 2p region of an as-deposited ZrO_2 thin film and after various post deposition anneals.

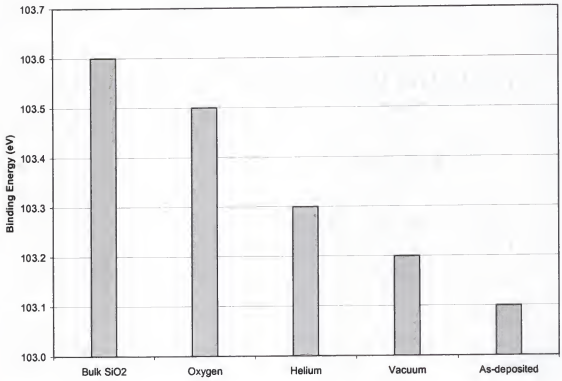

Figure 3-7 Plot of Si 2p binding energy of oxygen bonded to silicon as a function of oxygen content in the annealing system. Bulk SiO_2 has been added as a reference.

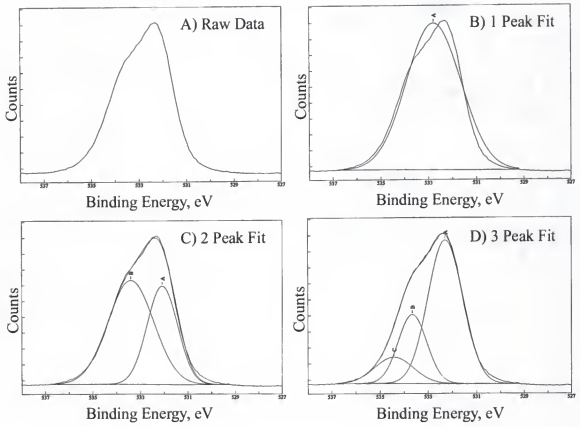

Figure 3-8 XPS spectra of A) raw data, B) 1 peak fit, C) 2 peak fit, and D) 3 peak fit fit illustrating the importance of a good model when analyzing XPS data.

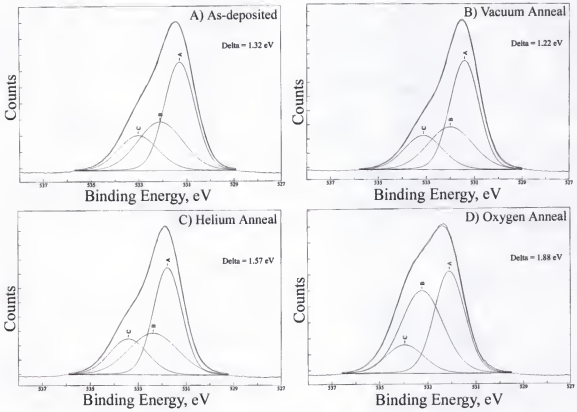

Figure 3-9 XPS spectra with "3 peak fit" of A) as-deposited, B) vacuum annealed, C) helium annealed, and D) oxygen annealed ZrO_2.

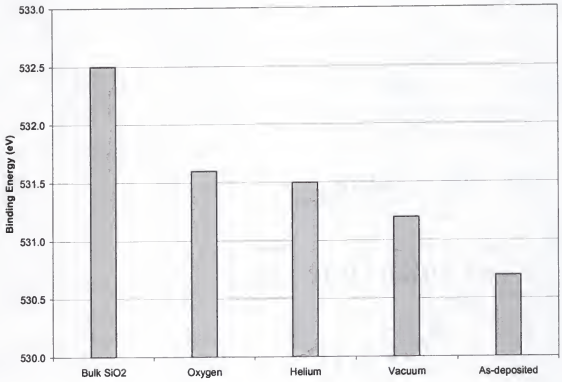

Figure 3-10 Plot of O 1s binding energy of oxygen bonded to silicon as a function of oxygen content in the annealing system. Bulk SiO_2 has been added as a reference.

CHAPTER 4
ULTRAVIOLET PROCESSING

Among the results from the experimentation with ZrO_2 post deposition anneals it was determined that even the as-deposited sample which did not undergo any additional processing already exhibited an interfacial layer. At that stage the interfacial layer was determined to have the smallest fraction of detrimental SiO_2 mixed with ZrO_2 compared to any later stages of processing, but exhibited the greatest amount of trapped oxygen. Since analysis of the interfacial layer revealed that further heat treatments resulted in the migration of the trapped oxygen to the interface, this portion of experiments aimed to investigate the possibility of reducing the amount of trapped oxygen in an as deposited dielectric film through the application of ultraviolet radiations sources. Additionally, this experimentation sought to determine if there were any other effects that occurred when ultraviolet radiation was utilized in-situ during deposition. A low pressure mercury lamp array was added to the conventional PLD system for in-situ ultraviolet-assisted deposition.

In-situ Ultraviolet PLD

A conventional PLD system was fitted with an array of low pressure mercury lamps. Both barium strontium titanate (BST) and yttrium oxide (Y_2O_3) samples were deposited for this study. Barium strontium titanate is an extremely high dielectric constant material with reported bulk values ranging from as low as 80 to as high as 3600 in bulk material depending on crystallographic orientation [57]. To date, BST has been rejected as a possible candidate for MOS applications due to its predicted unstable interface and the

predicted negative conduction band lineup when in direct contact with silicon. However, it still has been studied here due to previous results that indicate positive MOS results, and based on its merit as a possible high-k dielectric material in a device that does not have such stringent interfacial requirements as a MOS device does. Y_2O_3 has also been identified as a possible candidate for an alternate dielectric material, but not fully embraced because of its moderately high dielectric constant of ~10. If pursued, it would only provide a solution for a limited number of device generations before encountering the same problems SiO_2 is facing now. In this study, the paramount matter was to investigate possible effects the ultraviolet radiation may have with respect to properties of the deposited film, and specifically how oxygen is present in the system.

Barium Strontium Titanate (BST)

Two BST thin film samples were deposited for this study. One sample was deposited in the conventional PLD setup while the second was deposited under the UVPLD conditions where the low pressure mercury lamp array was utilized. For each case, the samples were deposited at a substrate temperature of 650 °C, at a pulse count of 800, and a laser fluence of ~1 J/cm^2. The optimum pressure was determined for each of the two samples by growing several samples at different pressures, performing x-ray diffraction (XRD) and then comparing the full width at half maximum (FWHM) values of the primary (110) peaks. The pressure that resulted in the smallest value for FWHM of the major XRD peak was determined to be the most crystalline and used for all subsequent experimentation. For BST, the sample deposited without ultraviolet radiation had an optimum oxygen deposition pressure of 20 mTorr, while the optimum pressure for the sample deposited with ultraviolet radiation had an optimum pressure of only 10 mTorr. This turns out to be a very important result that will be discussed in more detail later.

Under the above mentioned deposition conditions, samples were deposited and measured by VASE using a single layer model of barium titanate on silicon. Though the deposited samples were actually $BaSr_{0.5}Ti_{0.5}O_3$, the model for barium titanate was the closest model available and would exhibit similar optical properties to the BST. Any attempt to use a two layer model with an additional interfacial layer returned to a single layer model when the fitting program was executed. The resulting overall thickness values from the single layer model were 475Å and 415Å for UVPLD and PLD deposited samples, respectively. These values were used as the first approximations in XRR modeling.

The XRR plots for the PLD and UVPLD deposited samples are shown in Figure 4-1 and the data for each is shown in Table 4-1.

Table 4-1: XRR data for the PLD and UVPLD deposited BST samples.

PLD Sample	Thickness (Å)	Roughness (Å)	Density (g/cm^3)
Silicon Substrate		11	2.33
Interfacial Layer	34	9	3.26
BST	374	8	5.45
Surface Layer	18	6	3.7
UVPLD Sample			
Silicon Substrate		8	2.33
Interfacial Layer	33	6	3.45
BST	436	7	5.46
Surface Layer	5	25	2.19

The first important aspect to note in from Table 4-1, is that proper fitting of the BST required a "3 Layer Model" to fit the experimentally acquired data. In instances where a good fit cannot be readily found with a "2 Layer Model", an additional lower density layer may be added to take into account for surface impurities and roughness effects. The shape of the XRR plots of the BST, shown in Figure 4-1, revealed compelling evidence

for the existence of an interfacial layer for both the PLD and UVPLD deposited samples. The plot labeled "UVPLD Raw Data" shows a dampened region from ~0.425 to ~0.675° along the theta-2theta axis where the amplitude of the oscillations did not match all of the other values along the theta-2theta axis. The only method to account for this type of dampening is with the addition of an interfacial layer exhibiting a particular thickness and density combination. The plot labeled "UVPLD 1 Layer Model" shows how the oscillations remain constant along the entire theta-2theta axis without the addition of the interfacial layer. Sections C and D of Figure 4-1 show the best fits that could be achieved with the "3 Layer Model" for the UVPLD and PLD deposited samples, respectively. In the case of the PLD deposited sample, the thickness of the interfacial layer was ~34 Å whereas the UVPLD sample was 33 Å. More importantly, the density of the PLD deposited sample was ~3.26 g/cm^3 whereas the UVPLD was ~3.45 g/cm^3. This value is greater than that of a pure amorphous SiO_2, but still much less than a pure silicate or silicide. Another important characteristic to note included the high surface roughness of 25 Å associated with the UVPLD sample versus the only 6 Å for the PLD sample. Finally, the overall thicknesses from XRR are in good agreement with the earlier values determined from VASE.

In order to verify the existence of the interfacial layer seen in the XRR results, an XTEM micrograph of a BST film was obtained and is shown in Figure 4-2. The features of the micrograph include a two layered structure composed of a polycrystalline BST layer atop an amorphous interfacial layer atop the single crystalline silicon. Though the polycrystallinity of the BST layer is not apparent in Figure 4-2, less magnified images do in fact reveal the polycrystalline morphology.

In an effort to verify the large roughness differences found between the PLD and UVPLD deposited samples, atomic force microscopy (AFM) measurements were made on the samples. Seen in Figure 4-3, it was found that the AFM measurements made over an area of 1μm x 1μm verified the XRR results showing RMS values of 7Å to 23Å for PLD and UVPLD deposited samples, respectively. The AFM measurements also revealed a great deal of surface texturing associated with the UVPLD deposited sample with an average grain size of ~300 nm. This is in contrast to the PLD sample which exhibits neither surface texturing nor large grains.

The data for the XRD investigation of both the UVPLD and PLD deposited samples are shown in Table 4-2.

Table 4-2: XRD peak data for the PLD and UVPLD deposited BST samples.

PLD Sample	2-Theta Peak Location (°)	FWHM (°)	Peak Orientation
Peak 1	31.70	0.5573	(110)
Peak 2	45.45	0.5568	(111)
UVPLD Sample			
Peak 1	31.81	0.4705	(110)
Peak 2	45.61	0.5691	(111)

The XRD spectra were composed of two distinct peaks for each. The main difference between the PLD and UVPLD deposited samples was the slightly smaller (~0.0816° less) FWHM value in the (110) peak for the UVPLD deposited sample. An additional difference between the two samples is a slight shift in the 2-theta values between the PLD and UVPLD samples. These differences were attributed to both the grain size increase seen in the UVPLD sample as well as stresses inherent in the thin film system. A variation of XRD, grazing incidence x-ray diffraction (GIXD), was also completed for

the two samples. The GIXD plots are shown in Figure 4-4 and the data is shown in Table 4-3.

Table 4-3: GIXD peak data for the PLD and UVPLD deposited BST samples:

PLD Sample	2-Theta Peak Location (°)	FWHM (°)	Peak Orientation
Peak 1	31.74	0.5292	(110)
Peak 2	39.10	0.5481	(111)
Peak 3	45.68	0.6273	(200)
Peak 4	51.18	0.5850	(210)
Peak 5	56.55	0.6997	(211)
Peak 6	66.28	0.7341	(220)
UVPLD Sample			
Peak 1	31.84	0.5172	(110)
Peak 2	39.27	0.5281	(111)
Peak 3	45.53	0.6692	(200)
Peak 4	51.30	0.7095	(210)
Peak 5	56.67	0.6256	(211)
Peak 6	660.47	0.6930	(220)

Due to the different manner in which a GIXD plot is acquired, there are 6 distinct peaks associated with the scan. Matching the scans to the JCPDS diffraction file the scan indicates a good quality cubic $Ba_{0.5}$ $Sr_{0.5}TiO_3$. with all listed peaks in the JCPDS being accounted for in the spectrum. Inspection of the 2-theta positions of the peaks indicates slight shifting of the peaks to higher values for four out of the six orientations when ultraviolet radiation was used during processing. This shift was also accompanied by lower FWHM values for all of the associated orientations. Two of the six orientations, the (200) and (210), shifted to lower 2-theta values and were accompanied by higher values of FWHM.

The XPS data was taken without any sputtering and at a take-off angle of 90°. The plots of the O 1s region revealed a need for three peaks to properly fit the experimentally

acquired data. The binding energies associated with the peaks are A) ~530.1, B) ~532.0, and C) ~533.5 eV for oxygen bound to barium, oxygen physically trapped, and other surface impurities, respectively. A detailed inspection of peak B shows the key difference between the PLD and the UVPLD technique. As seen in Figure 4-5, with the application of the UV radiation, the amount of trapped oxygen is reduced from a value of ~15% to a value of only ~10%. This is of particular importance since the application of ultraviolet radiation during deposition results in less trapped oxygen available in the material that is available to migrate to the interface and react.

Two additional samples were deposited under identical conditions with the exception of a lower pulse count of 500. The resulting thickness as determined by VASE and XRR were 250 Å and 232 Å for UVPLD and PLD deposited samples, respectively. This pair of samples was made into MOS devices so differences in the electrical properties could be determined. To properly determine a good device for testing, current-voltage measurements were made on the two samples. Figure 4-6 shows a plot of current density versus voltage and that both of the samples exhibited very low leakages of $1x10^{-4}$ A/cm^2 over a wide range of voltages from minus 3 to positive 1.5 volts. The high frequency capacitance versus voltage plot is shown in Figure 4-7. It shows how the accumulation capacitance associated with the UVPLD deposited sample is enhanced compared to that of the PLD deposited sample. With a dot size of $8.08x10^{-8}$ m^2 the capacitances associated with the PLD and UVPLD deposited samples are 662 pF and 790 pF, respectively. Using equation 1-7, the equivalent oxide thickness of the conventionally grown PLD sample is reduced from an actual thickness of 232 Å to an EOT of 42 Å. More importantly, the UVPLD sample reduced from an actual thickness of 250 Å to and

EOT of 35 Å! These relatively low EOT values are a result of overall dielectric constant calculations of 21.5 and 27 for the PLD and UVPLD deposited samples, respectively. This represents a 25.5% increase in dielectric constant with the application of ultraviolet radiation.

For the in-situ UVPLD study of BST, VASE measurements were completed for a base measurement of thicknesses that were input as a starting value for XRR modeling. The XRR revealed two important findings. The first was the existence of an interfacial layer with a density greater than that of pure SiO_2 and the second was a large surface roughness associated with the UVPLD deposited sample, but not the PLD deposited sample. An XTEM investigation verified that indeed there was an amorphous interfacial layer while AFM verified that the UVPLD deposited sample exhibited a great deal of texturing with large ~300 Å grains. The increased texturing was also indicated in the XRD and GIXD through more intense peaks with lower FWHM values for certain peaks while others became less intense with larger FWHM values. XPS was able to discern a reduction in the amount of physically trapped oxygen associated with the UVPLD deposited sample. Reasoning for this lower amount of trapped oxygen stems from the lower oxygen pressure that is enabled during a UVPLD deposition as a result of the addition of the ultraviolet radiation sources. This lower amount of oxygen can also explain the greater density seen in the interfacial layer for the UVPLD deposited sample since the ratio of SiO_2 to BST would be less. Finally, capacitance voltage measurements revealed an enhanced dielectric constant and low EOT values for the UVPLD deposited sample. While the low EOT values were not less than the current 18 Å SiO_2 layer used, it did clearly illustrate two important notions. First, it shows how a high dielectric constant can

take a thick (relatively speaking) layer not subject to tunneling leakage issues and allow it to perform like an ultrathin layer. Secondly, it illustrates the important role that ultraviolet radiation can play in achieving high quality dielectrics when deposited under more reactive oxygen conditions.

All of the above mentioned results question the claim that BST is a poor selection as an alternative dielectric material because of its thermodynamic instability with silicon and its lack of a conduction band barrier. The answers to these two questions are as follows: The calculations for band offsets generated by Robertson [5] were made for a given dielectric when in an ideal direct contact with silicon. However, it was mentioned that if there were some type of buffer layer between a dielectric and the silicon that this would change the band offset properties. This is what had happened with the BST. As seen in the XTEM image of BST, there is clearly an interfacial layer that had formed. As an extension of the results from the ZrO_2 study, it is reasonable to conclude that the BST had also generated an interfacial layer that was composed of a physical mixture of SiO_2 and BST. With this extension, the band offset associated with the structure would be intermediate between the value of BST in direct contact with silicon and that of SiO_2 in direct contact with silicon thus eliminating that issue. Similarly, the lack of thermodynamic stability of BST in direct contact with silicon is also questionable since the interface is in fact an interfacial layer that is partially SiO_2. It is the unusually high dielectric constant of BST that still allowed the multilayered system to generate such good dielectric constant values and low equivalent oxide thicknesses. It also follows that if the interfacial layer had even less SiO_2 or was physically thinner, the effect of the low-k layer would be less pronounced allowing even better results. With respect to the

structural changes seen in the data, energetic photon bombardment of the surface would most rationally explain these results. More importantly, the fact that the ultraviolet radiation is acting in an in-situ manner allows the photons to continually interact with each atomic layer as the structure is deposited. This added energy could account for the structural differences noted.

For the BST, ultraviolet radiation has been used to modify chemical properties of the thin film system by reducing the amount of trapped oxygen in the deposited layer. Less trapped oxygen in the structure during deposition and cooldown dictates less possible migration of oxygen species to the interface during deposition and post deposition processes resulting in less negative effects with respect to the interfacial layer. The effect of energetic photons that impinge each layer of the material during deposition can account for the structural changes that were noted in the crystallinity and roughness. The combined effect of the chemical and structural changes resulted in enhanced electrical properties with good leakage currents and low EOT values. It is concluded that due to a more controlled oxygen environment, as a result of application of ultraviolet radiation, higher quality samples can be deposited which exhibit superior structural, chemical and electrical properties.

Yttrium Oxide (Y_2O_3)

Ultraviolet radiation studies were also conducted for yttrium oxide. While it has been passed over by many research teams as a possible alternative dielectric layer, most of the rationale for this decision is due to the theoretical dielectric constant of ~10 that Y_2O_3 exhibits. In this case, replacement of SiO_2 would only be effective for a few generations before Y_2O_3 faced many of the same issues that SiO_2 faces today. Regardless, it has been studied here in an attempt to determine the effects of ultraviolet

radiation on an additional oxide material that satisfies the criteria for a good candidate. To start the investigation, samples were grown in a similar manner as the BST whereby optimum growth pressures were determined for a given growth temperature. In this case, the Y_2O_3 thin films were grown for a pulse count of 300 at a temperature of 400 °C and an oxygen pressure of 4 mTorr and 10 mTorr for UVPLD and PLD, respectively. Once again, an array of low pressure mercury lamps was used in-situ during the deposition for the UVPLD deposited sample.

VASE investigations of the UVPLD and PLD deposited samples measured overall thicknesses of ~85 Å and ~76 Å, respectively. Much like the ZrO_2 and BST samples, a single layer model was the most appropriate for modeling the data. This is once again attributed to the inability of VASE to discern additional layers without returning to a single layer approximation, but not necessarily an indication that there is not actually a second layer present.

The XRR plots are shown in Figure 4-8 and the data from the model is shown in Table 4-4.

Table 4-4: XRR data for the PLD and UVPLD deposited Y_2O_3 samples.

PLD Sample	Thickness (Å)	Roughness (Å)	Density (g/cm^3)
Silicon Substrate	∞	5	2.33
Interfacial Layer	16	6	2.27
Y_2O_3	50	3	5.03
Surface Layer	5	4	3.61
UVPLD Sample			
Silicon Substrate	∞	5	2.33
Interfacial Layer	15	4	2.52
Y_2O_3	56	5	5.03
Surface Layer	7	4	3.60

A 3 layer model was used to fit the experimental data. This created in similar results to the BST study with the need for an interfacial layer in the modeling to appropriately describe the acquired data. The interfacial layer for the UVPLD deposited sample exhibited a density of ~2.52 g/cm^3 whereas the density of the PLD deposited sample was a lower value of ~2.27 g/cm^3. Both of these interfacial layers had a density greater than that of pure amorphous SiO_2 and less than that of any type of yttrium silicate or silicide.

An XTEM micrograph was obtained for the Y_2O_3 system to determine if an interfacial layer was present. As shown in Figure 4-9, the Y_2O_3 exhibited a polycrystalline Y_2O_3 layer atop an amorphous interfacial layer atop the single crystalline silicon. This result is comparable to the ZrO_2 and BST results previously shown. The XTEM image also showed a columnar structure associated with the polycrystalline Y_2O_3 film. This was the case for both PLD and UVPLD grown samples.

An investigation of the crystallinity of the two samples by GIXD, seen in Figure 4-10, revealed a single peak associated with Y_2O_3 that is described in Table 4-5.

Table 4-5: GIXD peak data for the PLD and UVPLD deposited Y_2O_3 samples

PLD Sample	2-Theta Peak Location (°)	FWHM (°)	Peak Orientation
Peak 1	30.34	1.3052	(222)
UVPLD Sample			
Peak 1	30.21	1.8045	(222)

GIXD was chosen over XRD for this set of experiments since the thickness of the layer was quite low and GIXD would be a more effective mode to observe meaningful differences in the resulting peaks. A single peak that corresponded to a (222) oriented cubic Y_2O_3 layer was present. The FWHM value for the UVPLD deposited sample was smaller than the PLD deposited by ~0.493° which is once again an indication of larger

gain sizes. Additionally, the position of the (222) peak shifted ~0.13° indicating stresses associated with the thin film system. Inspection of Figure 4-9 will reveal that there are additional peaks located around ~50 -55°, but these peaks have all been attributed to silicon peaks such as the (311).

Inspection of the XPS data also reveals a similar result as the BST. In the case of the Y_2O_3, the O 1s peaks, shown in Figure 4-11, the asymmetric peak can be deconvoluted into two distinct peaks. Peak A is located at ~529.1 eV and peak B is located at ~530.9 eV. Peak A located at 529.1 eV corresponds to yttrium bound to oxygen while peak B located at ~530.9 eV corresponds to trapped oxygen in the layer. Similar to the BST, there is a clear reduction in the amount of trapped oxygen with the application of ultraviolet radiation. The value reduces from ~20% trapped in the conventional PLD grown sample to ~10% in the UVPLD sample.

It is thus shown once again how ultraviolet radiation played a direct role in altering the chemical properties of the oxide system reducing the amount of trapped oxygen within the Y_2O_3 structure. Once again, similar to BST, XRR investigations revealed the need for an interfacial layer with a greater density than pure amorphous SiO_2 to properly fit the XRR spectra. The interfacial layers existence was verified by XTEM while GIXD indicated marginal differences in grain structure and/or internal film stresses. XPS investigations showed how ultraviolet radiation during deposition allowed for lower ambient oxygen pressures which resulted in a marked reduction of trapped oxygen in the films.

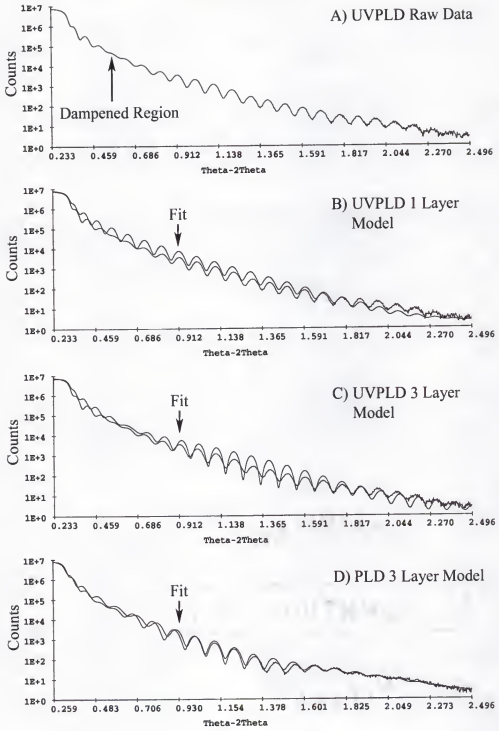

Figure 4-1 XRR spectra of A) UVPLD raw data, B) UVPLD 1 layer model, C) UVPLD 3 layer model, and D) PLD 3 layer model for BST samples.

Figure 4-2 Cross sectional TEM of a polycrystalline BST thin film atop an amorphous interfacial layer atop a single crystal silicon substrate.

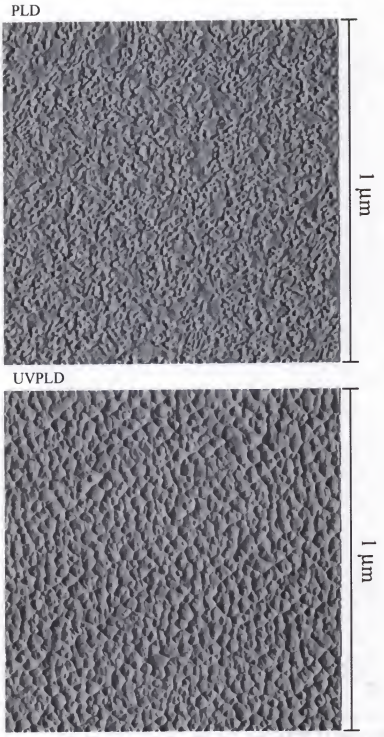

Figure 4-3 AFM of BST for PLD and UVPLD deposited samples. The UVPLD deposited sample exhibits increased roughness larger grain sizes.

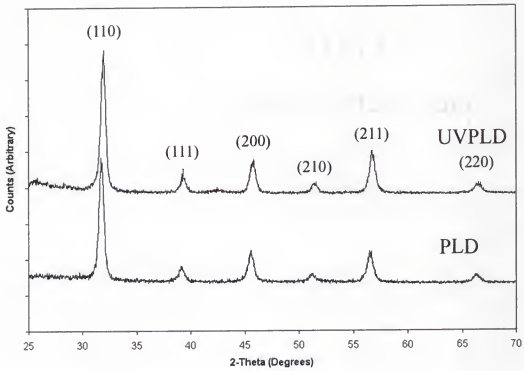

Figure 4-4 GIXD of BST for PLD and UVPLD deposited samples. The UVPLD deposited sample exhibits increased (110) texturing.

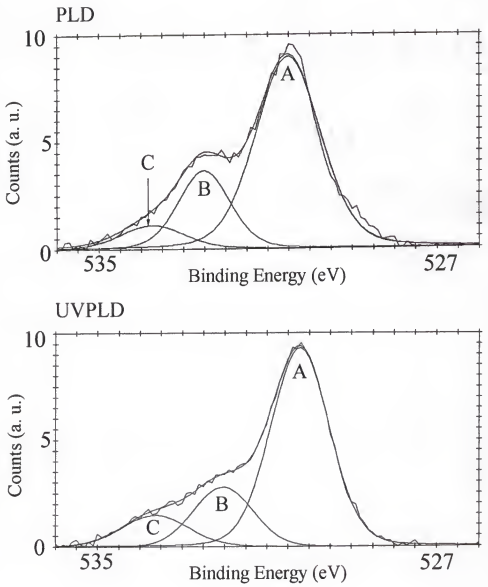

Figure 4-5 O 1s XPS of BST for PLD and UVPLD deposited samples. Peak B corresponds to the amount of physically trapped oxygen in the thin film structure and is reduced in the UVPLD deposited sample.

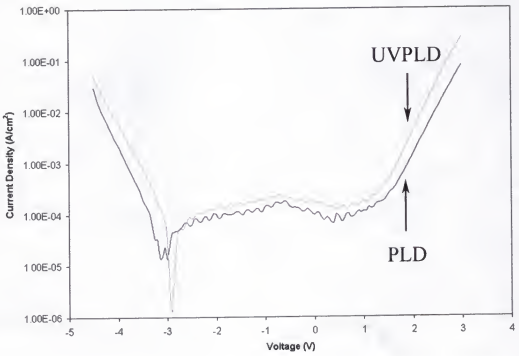

Figure 4-6 Current density versus voltage plot for BST of PLD and UVPLD deposited samples.

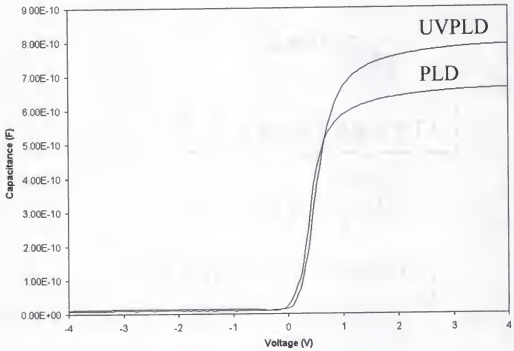

Figure 4-7 High frequency capacitance versus voltage plot for BST of PLD and UVPLD deposited samples.

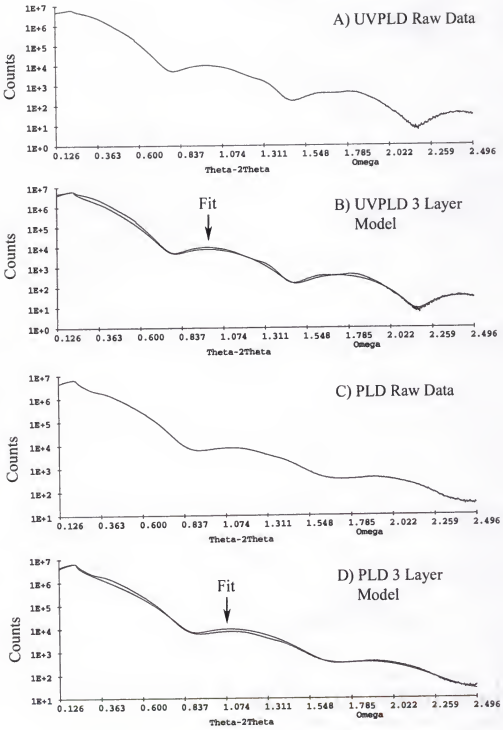

Figure 4-8 XPS spectra of A) UVPLD raw data, B) UVPLD 3 layer model, C) PLD raw data, and D) PLD 3 layer model for Y_2O_3 samples.

Figure 4-9 Cross sectional TEM of a polycrystalline Y_2O_3 thin film atop an amorphous interfacial layer atop a single crystal silicon substrate.

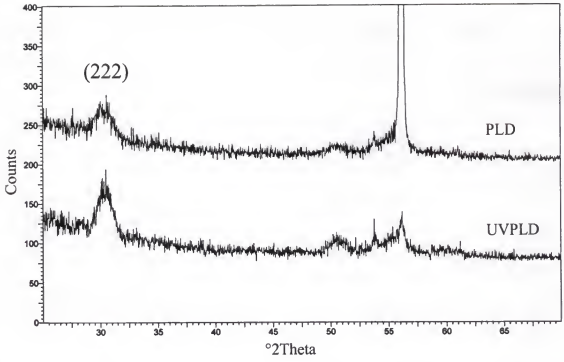

Figure 4-10 GIXD of Y_2O_3 for PLD and UVPLD deposited samples. The UVPLD sample exhibits increased (222) texturing.

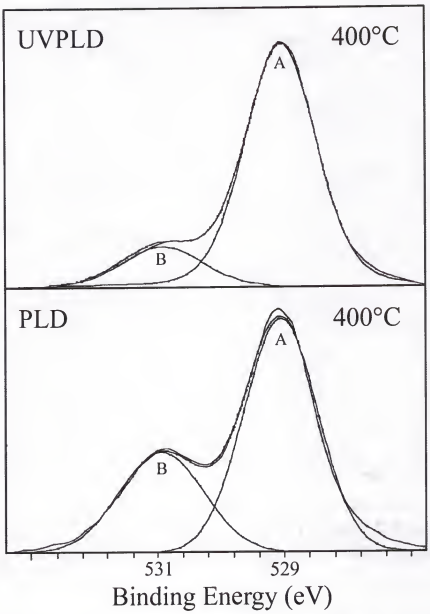

Figure 4-11 O 1s XPS of Y_2O_3 for PLD UVPLD deposited samples. Peak B corresponds to the amount of physically trapped oxygen within the thin film structure.

CHAPTER 5
POST DEPOSITION ULTRAVIOLET ANNEALING

The final area of research related to the post deposition annealing of HfO_2 thin films. In this experimentation, the goal was to determine if there were any ultraviolet effects that resulted from adding an ultraviolet radiation source to post deposition oxygen anneal. Since the films were amorphous and particularly thin, there were several possibilities that could occur. The first was that the oxygen would directly react with the HfO_2 amorphous network to better oxygenate the film. The next was the possibility of the high energy photons being emitted from the lamp changing the structural characteristics (amorphous to crystalline) of the films. Finally, there was the possibility of oxygen passing directly through the films and reacting with the silicon at the interface and growing an SiO_2 interfacial layer.

Ultraviolet-Assisted Oxidation of Silicon

Since the ultraviolet radiation source for this portion of the experimentation was the home built silent barrier discharge excimer lamp, a preliminary test to verify the effect of ultraviolet radiation and its ability to generate atomic oxygen and ozone was completed. In this study, a series of samples had their native SiO_2 layer removed by a dip in 1 % hydrofluoric acid for 10 minutes. They were then immediately loaded into a high vacuum system equipped with the excimer ultraviolet radiation source. Two sets of four samples were processed whereby the samples were oxidized for 30, 60, 90, and 120 minutes in 5 mTorr of oxygen at 300 °C with and without ultraviolet radiation present. At this temperature dry oxygen annealing was not expected to generate a SiO_2 layer of

any appreciable thickness. In contrast, previous work by Boyd et. al. [29] indicated that if intense ultraviolet radiation was being emitted from the excimer source, dry oxygen would be converted into atomic oxygen and ozone which would lead to appreciable oxidation of the silicon. The results are displayed in Table 5-1 and shown graphically in Figure 5-1.

Table 5-1 VASE thickness measurements for silicon oxidized with and without ultraviolet radiation at 300°C.

Time (minutes)	Thickness (Å)	UV Thickness (Å)
30	5	35
60	6	46
90	7	56
120	7	63

VASE measurements verified that indeed, there was not appreciable oxidation of the silicon with dry oxygen annealing where the greatest thickness of SiO_2 was only 7Å for the longest duration anneal. As a comparison, the sample annealed in the presence of ultraviolet radiation for the same time duration was oxidized to 63Å. This nine-fold increase in thickness verified that the excimer source was working properly.

HfO_2 Post Deposition Anneal

Since the oxidizing effectiveness of the ultraviolet source had been proven, HfO_2 samples were annealed at various temperatures with and without ultraviolet radiation. The goal was to determine the role that UV radiation could play in a post deposition anneal versus using a dry oxygen anneal. The samples were grown by Motorola Corporation by a chemical vapor deposition setup and delivered directly for analysis (i.e., the samples did not undergo any of the "typical" densification anneals). The samples were amorphous and grown to a thickness of ~55Å of which, ~10Å was attributed to an interfacial layer. This data was supplied by Motorola without additional elaboration

about their deposition or measurement techniques. Seven samples were processed for this experimentation. One sample was set as an as-deposited control sample, while the other six samples were annealed at 300, 475, and 600°C in 5 mTorr of oxygen with and without ultraviolet radiation. XRD, GIXD, AFM, VASE, XRR, and capacitance-voltage measurements were conducted on these samples.

XRD of the as-deposited control sample showed that the structure of the films was amorphous. That is, there were not any distinguishable peaks typically associated with a crystalline HfO_2 structure. More importantly, none of the samples that underwent post deposition heat treatments showed any diffraction peaks. This indicates that all of the HfO_2 films regardless of whether ultraviolet radiation was present retained their amorphous character. GIXD was also conducted as a secondary check to this finding since the films were quite thin. GIXD also revealed retention of the amorphous state throughout all anneal conditions with and without ultraviolet radiation.

AFM measurements were conducted and, unlike in-situ UV irradiation, there were no changes found, such as texturing, in the surface morphology. All samples exhibited a random morphology with RMS roughness values in the 5 - 7 Å range. This was consistent with the lack of crystallinity noted in the samples from the XRD and GIXD data. All of these findings indicate that there were not any structural changes associated with the HfO_2 system.

VASE measurements were made for each of the anneal conditions and are shown in Table 5-2. From Figure 5-2, it can be seen that dry oxygen annealing did not result in an increase of the overall thickness of the HfO_2 layer for any of the anneal temperatures.

Table 5-2 VASE thickness measurements for HfO_2 anneals with and without ultraviolet radiation.

	Temperature (°C)	Thickness (Å)	Excimer Ultraviolet Radiation
Sample 1	As-deposited	52	--
Sample 2	300	53	NO
Sample 3	475	52	NO
Sample 4	600	53	NO
Sample 5	300	56	YES
Sample 6	475	59	YES
Sample 7	600	64	YES

On the other hand, the anneals conducted with excimer ultraviolet radiation continually increased in thickness from a starting value of ~53Å for the as-deposited sample to a value of ~64Å for the 600°C anneal. These values were used as a first approximation in the XRR modeling.

XRR measurements of the samples indicated slight differences in the thickness of the total film thickness that compared well with the values seen in the VASE measurements. A "3 Layer Model" was used for the interpretation since an interfacial layer was required for good model fits to be found. The thickness of the HfO_2 layer remained relatively constant, but there were distinct variations in the thickness and density of the interfacial layer. These variations are presented in Table 5-3 and shown in Figures 5-3 and 5-4.

Figure 5-3 clearly shows that the samples annealed in dry oxygen had only a marginal increase in the thickness of the interfacial layer, but only for the sample that was annealed at the highest temperature. However, those samples annealed in the presence of ultraviolet radiation had an increase in the interfacial layer thickness even for the 300 °C anneal. The samples that were annealed at higher temperatures had more substantial increases in the thickness of the interfacial layer. Figure 5-4 shows that the density of the interfacial layer is at its highest value for the as-deposited sample and that any subsequent

Table 5-3 XRR data for the thickness and density of the amorphous interfacial layer.

	Temperature (°C)	Excimer Ultraviolet Radiation	Interfacial Layer Thickness (Å)	Interfacial Layer Density (g/cm^3)
Sample 1	As-deposited	--	15	2.84
Sample 2	300	NO	15	2.79
Sample 3	475	NO	15	2.67
Sample 4	600	NO	16	2.42
Sample 5	300	YES	18	2.71
Sample 6	475	YES	20	2.50
Sample 7	600	YES	23	2.34

heat treatments corresponded to decreases in the density. The samples that were annealed in the presence of ultraviolet radiation decreased in density faster than the dry oxygen anneal samples for all of the anneal temperatures. For example, the density of the sample annealed at 475 °C without ultraviolet radiation had a density of 2.67 g/cm^3 while the sample annealed with ultraviolet radiation at the same temperature had decreased to 2.5 g/cm^3.

Capacitance voltage measurements were made on all samples. As mentioned previously, the accumulation capacitance will be a function of the HfO_2 and any interfacial layers that are present in the system. If there is a change in the oxygen environment in the system, this will be reflected in the accumulation capacitance of the whole system. Capacitance-voltage results for the system are shown in Figure 5-5. It can be seen that the as deposited sample exhibited the greatest value of accumulation capacitance. All subsequent anneals resulted in a decrease in the accumulation capacitance. The accumulation capacitance of the samples that were annealed in the presence of ultraviolet radiation decreased more quickly than the dry oxygen annealed samples for any given temperature.

In summary, structural analysis was completed in the form of XRD, GIXD and AFM. For each of these analyses, there were not any measurable differences between the as-deposited sample and any of the annealed samples. XRD and GIXD verified retention of the amorphous state of the HfO_2 and AFM showed no changes in the morphology of the surface. VASE was used to determine an overall thickness that was used as the starting points for XRR investigations. XRR verified the existence of an interfacial layer and showed that as the annealing temperatures increased, variations in the density and thickness of the interfacial layer occurred. The important ramification of this finding was that the samples annealed in the presence of ultraviolet radiation decreased in density more rapidly than the dry oxygen annealed samples while the thickness of the interfacial layer increased more rapidly than the dry oxygen annealed samples. Capacitance-voltage measurements exhibited the highest accumulation capacitance for the as deposited sample and all subsequent anneals resulted in lower accumulation capacitances as a function of temperature and ultraviolet illumination.

The explanation for these results relates to the ability of the ultraviolet radiation to convert dry oxygen to atomic oxygen and ozone. The atomic oxygen can migrate more easily within the HfO_2 structure. This ability to easily migrate accompanied by increasing temperature allows the oxygen to migrate to the silicon interface, react, and form SiO_2. In the as-deposited sample, the density of the interfacial layer is greatest since there has not been any additional oxygen added to the system. That is, the mixture of SiO_2 and HfO_2 that exists has the smallest fraction of SiO_2 at this stage. Any additional anneals increases the SiO_2 fraction resulting in decreasing the density to values that are closer to pure SiO_2 as well as contributing to the growth of the interfacial layer

overall. This growth of the interfacial layer manifests itself readily in the electrical characterization where the low-k dielectric layer plays an increasingly important role.

The main conclusions from this study are that post deposition annealing in an oxygen ambient will have a detrimental effect on the electrical properties of the device. The application of ultraviolet radiation amplifies the problem by creating more mobil highly reactive oxygen species that can move easily to the interface and react with silicon. If there are any beneficial oxygenation effects that occur within the HfO_2 layer, their benefit is quickly nullified by the detrimental effects of the low-k interfacial layer that develops during the heat treatments.

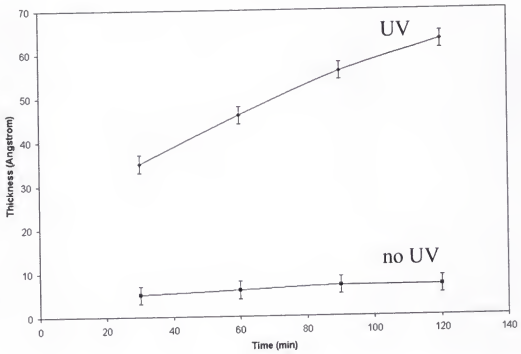

Figure 5-1 VASE thickness versus time results for oxidation of silicon with and without excimer radiation in oxygen.

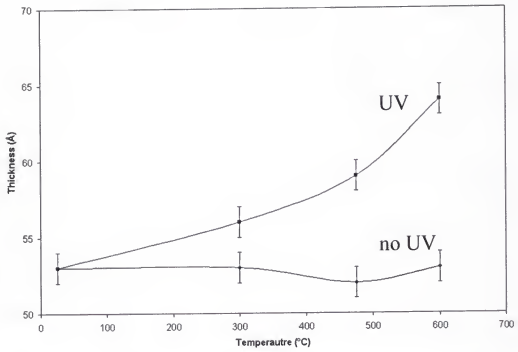

Figure 5-2 VASE thickness of the overall HfO_2 for samples annealed with and without ultraviolet radiation.

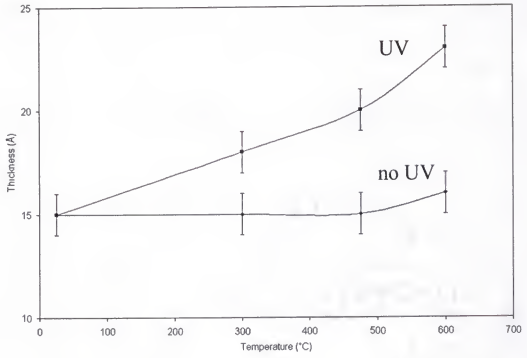

Figure 5-3 XRR thickness measurements of the HfO_2 interfacial layer for samples annealed with and without ultraviolet radiation.

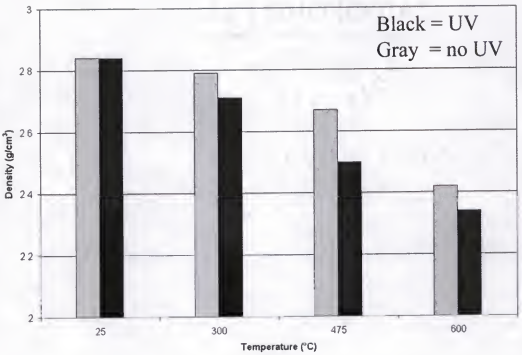

Figure 5-4 XRR density measurements of the HfO_2 interfacial layer for samples annealed with and without ultraviolet radiation.

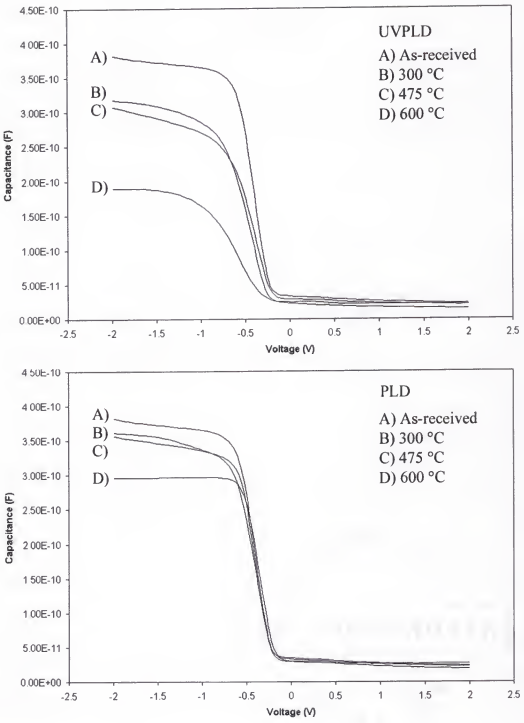

Figure 5-5 Capacitance-voltage measurements of HfO_2 MOS devices for samples annealed with and without ultraviolet radiation.

CHAPTER 6
CONCLUSIONS

Since SiO_2 will be unable to continue as the dielectric material of choice in MOSFET device structures, there exists a driving force to replace the existing SiO_2 layer with an alternative layer with a higher dielectric constant. Though many research teams have investigated numerous different materials in an attempt to accomplish this goal, to date, none have succeeded due to new problems associated with the insertion of the alternative layer. The more prominent of these issues include the formation of an unwanted low-k interfacial layer that forms between the silicon substrate and the dielectric material as well as excessive leakage currents. The studies associated with this dissertation addressed the issues related to these two problems as they are related to oxygenation in the growth system.

First, experimentation was conducted whereby ultrathin ZrO_2 samples were deposited and exposed to low, medium, and high oxygen annealing conditions at 750 °C. From the various characterization techniques, it was determined that the films deposited by pulsed laser deposition exhibited an interfacial layer even for samples that were not post-deposition annealed. Additionally, post deposition annealing under high vacuum conditions resulted in development of the interfacial layer and reduction of physically trapped oxygen in the film structure. FTIR analysis of post deposition annealed samples in helium and oxygen resulted in substantial increases in the Si—O bonding. The final conclusion from this portion of experimentation was that the interfacial layer is already formed during deposition. Subsequent annealing results in a migration of physically

trapped oxygen in the film to the interface that reacted wilh silicon and increased the SiO_2 content in the interfacial region. Since this amount of oxygen was limited, it was also concluded that oxygen in the ambient deposition gases also migrated to the interface to react with the interface.

In the second portion of experimentation, ultraviolet radiation from a low pressure Hg lamp was added to the conventional pulsed laser deposition system. The addition of ultraviolet radiation to the growth system was selected because of its ability to react with dry oxygen to create atomic oxygen and ozone. These species are more reactive than dry oxygen and, in the case of the atomic oxygen, can move easily through the lattice of a dielectric film. It was found from the optimization process for deposition of the BST and Y_2O_3 that UV radiation allowed for lower oxygen pressures to be used during deposition while still attaining high quality samples. The impact of this finding is of significant relevance because it results in less physically trapped oxygen in the deposited structures and less oxygen available for reaction during deposition. Additionally, it was found that several other properties such as texturing and electrical characteristics were altered with the application of UV radiation. It was found that there still existed an interfacial layer from deposition alone, but the characteristics of that interfacial layer were altered as a results of the different oxidizing species generated by the ultraviolet radiation. This played an important role in the growth of good quality films.

In the final portion of experimentation, already deposited HfO_2 thin films received from Motorola Corporation were exposed to excimer ultraviolet radiation. In doing so, It was found that the changes in structure that were seen for the in-situ irradiation did not occur for the post deposition annealed samples. Capacitance voltage measurements

indicated that there were more reactive species present in the ultraviolet annealed samples compared to the samples processed without ultraviolet radiation by the fact that the overall accumulation capacitances of the CV plots continually decreased. In this scenario, the oxygen species migrate immediately through the HfO_2 layer to the interface and add to the growth of the interfacial layer.

Studies in this dissertation indicated that there is development of an interfacial layer during deposition and that ultraviolet radiation could be beneficial to the growth system. The addition of UV radiation enhanced the properties of the thin film if used for in-situ deposition; however, it can also be detrimental with respect to devices if migrating species are allowed to migrate either from the film or from the ambient to the interface and react with silicon to further develop the low-k interfacial layer.

APPENDIX
ELECTRICAL DATA EXTRACTION METHOD

When conducting electrical characterization, once the proper model has been chosen for the with the Metrics ICS software, measurements may be acquired and a significant amount of information may be extracted from this data. For example, by calculating the total fixed charge in a MOS stack, numerous other important data are generated from the process. The derivation of the fixed charge will be done as an example.

It is important to first get a current-voltage measurement from one of the MOS devices to determine an appropriate diode to make capacitance-voltage measurements on. That is, a diode with a high breakdown voltage and turn on characteristics. Once this is determined, a high frequency/quasistatic output from the Win-82 system may be generated. A typical result for a p-type wafer is shown in Figure 2-11. While both curves are important, for this process, the calculations will be based off the high frequency curve. The first step is to use the CV curve to calculate doping concentration in the substrate. This is done by plotting the reciprocal of the square of the capacitance versus the gate voltage. The new plot should exhibit a linear region. By taking the slope of the linear region, it is possible to calculate the doping in the semiconductor. It is important to note that curvature in this region may represent nonuniform doping in the semiconductor. The equation for determining the doping is shown below:

$$N = \frac{2}{q\varepsilon_s A^2 (slope)} \qquad \text{(A-1)}$$

where q is the electric charge, ε_S is the semiconductor dielectric constant, A^2 is the gate area, and N is the doping (acceptor or donor). With the value, it is now possible to calculate the Debye length (L_D).

$$L_D = \sqrt{\frac{\varepsilon_S kT}{q^2 N}} \tag{A-2}$$

where k is the Boltzmann constant and T is temperature in Kelvin. With this value the semiconductor flatband capacitance can be calculated.

$$C_{FBS} = \frac{\varepsilon_S A}{L_D} \tag{A-3}$$

The next step is to calculate or experimentally determine the capacitance of the dielectric layer (C_i). In the scenario described here, the capacitance has been measured and represents the value of capacitance of the high frequency curve in the accumulation region. This typically is taken at a value of minimal leakage current, as ascertained by the previous IV measurements. If, one was unable to measure the capacitance, but had knowledge such as the thickness of the dielectric layer, d, area of the MOS stack, A, and the dielectric constant, ε_i, of the dielectric layer, then it is possible to calculate the corresponding capacitance of the insulator. The relationship is shown as follows:

$$C_i = \frac{\varepsilon_i A}{d} \tag{A-4}$$

The next important parameter in the process is calculation of the overall flatband capacitance:

$$C_{FB} = \frac{C_{FBS} C_i}{C_{FBS} + C_i} \tag{A-5}$$

and the ratio

$$\frac{C_{FB}}{C_i} \tag{A-6}$$

The next step is to calculate the V_{shift} this is done by plotting C/C_i versus gate voltage. Then use the ratio of $C_{FB}/C_i$to to visually determine the flatband voltage shift (ΔV_{shift}). In an ideal MOS capacitor, the flatband voltage condition corresponds to a $\Delta V_{shift} = 0$ thereby allowing the conclusion that any voltage shift should be related to total fixed charge. This charge may come from many different sources:

Q_m >	Mobile Charges	>	location dependent on bias
Q_{ot} >	Oxide Trapped	>	distributed in the oxide
Q_f >	Fixed Oxide	>	near surface charge
Q_{it} >	Interfacial Traps	>	at the interface

The first three of these charges causes shifts of the overall CV curve to the left or right while the fourth charge manifests itself as changes in slope (stretching) of the overall CV curve.

The next step is to determine the value ϕms, which is the work function of the metal minus the work function of the semiconductor. Depending on the wafer type used, this would be done as follows

p-type $$\phi_{MS} = \phi_M - \phi = \phi_M - \left[X + \frac{E_g}{2} + \Psi_B \right] \tag{A-7}$$

n-type $$\phi_{MS} = \phi_M - \phi = \phi_M - \left[X + \frac{E_g}{2} - \Psi_B \right] \tag{A-8}$$

where $E_g/2$ is the intrinsic Fermi level, ϕ_M is the metal work function, ϕ_S is the semiconductor work function, X is the electron affinity of the semiconductor, and Ψ_B is the Fermi level difference between the Fermi level and the intrinsic Fermi level.

Finally, the total oxide charge may be calculated with the following equation by collating all of the previously determined values as:

n-type $$N_f = \left[\frac{\Delta V - \phi_{MS}}{q}\right] C_i \qquad \text{(A-9)}$$

Another important electrical value that is commonly cited in literature is the value of the interface traps, Qit. There are several possibilities for determining this value: 1) comparison of the high frequency capacitance to a theoretical capacitance without any interface traps, 2) comparison of a low frequency capacitance to a theoretical capacitance without any interface traps, or 3) comparison of a high frequency capacitance to a low frequency capacitance. The third option, first developed by Castagné and Vapaille consisted of combining the low and high frequency curves (i.e., the output of the Win-82 system) to determine the silicon surface capacitance per unit area, C_S. Unlike the Terman method where only the high frequency capacitance (C_{HF}) is measured, or the Berglund method where only low frequency capacitance (C_{LF}) is measured, this method measures both C_{LF} and C_{HF}. This eliminates the need for the generation of any of the theoretical computations needed for the other methods. As outlined in more detail by Nicollan and Brews [65], the basic result is that interface trap level can be determined at a given voltage as a function of position in the bandgap by simple input of measured parameters into the following equation:

$$D_{it} = \frac{\Delta C}{q}\left(1 - \frac{C_{HF} + \Delta C}{C_{ox}}\right)^{-1}\left(1 - \frac{C_{HF}}{C_{ox}}\right)^{-1} \qquad \text{(A-10)}$$

where Dit is the interface trap density, C_{ox} is the capacitance per unit area, and

$$\Delta C = C_{HF} - C_{LF} \qquad \text{(A-11)}$$

This equation is used to make a plot if D_{ito} versus C_{HF}/C_{ox} where

$$D_{it} = D_{ito} \frac{1000}{x_o} \qquad \text{(A-12)}$$

and x_o is the thickness of the oxide in question. Combination of the directly measured CV data and the above equation it is therefore possible to determine the Dito. It is important to realize, however, that accurate values of Dit cannot be determined over the entire range of gate bias' due to a variety of reasons including round-off errors, errors due to use of a 1 Mhz CV curve, and error from C_{LF}. Each of these errors is addressed in detail in Nicollian and Brews.

LIST OF REFERENCES

1. S. M. Sze, *Physics of Semiconductor Devices*, 2nd ed. (Wiley, New York, 1981)

2. D. A. Buchanan: IBM J. Res. Develop. **43**, 245 (1999)

3. E. H. Nicollian, and J. R. Brews, *MOS (Metal Oxide Semiconductor) Physics and Technology* (Wiley, New York, 1982)

4. G. D. Wilk, R. M. Wallace, J. M. Anthony: J. Appl. Phys. **89** (10), 5243 (2001)

5. J. Robertson: J. Vac. Sci. Technol. B **18** (3), 1785 (2000)

6. K. J. Hubbard, D. G. Schlom: J. Mater. Res. **11** (11), 2757 (1996)

7. M. Copel, M. Gribelyuk, E. Gusev: Appl. Phys. Lett. **76** (4), 436 (2000)

8. M. Houssa, M. Naili, C. Zhao, H. Bender, M. M. Heyns, A. Stesmans: Semicond. Sci. Technol. **16**, 31-38 (2001)

9. M. E. Hunter, M. J. Reed, N. A. El-Masry, J. C. Roberts, S. M. Bedair: Appl. Phys. Lett. **76** (14), 1935 (2000)

10. S-K. Kang, D-H. Ko, E-H. Kim, M. H. Cho, C. N. Whang: Thin Solid Films **353**, 8 (1999)

11. S. J. Wang, C. K. Ong, S. Y. Xu, P. Chen, W. C. Tjiu, A. C. H. Huan, W. J. Yoo, J. S. Lim, W. Feng, W. K. Choi: Semicond. Sci. Technol. **16**, L13 (2001)

12. J. Gottmann, A. Husmann, T. Klotzbücher, E. W. Kreutz: Surf. Coat technol. **100-101**, 415 (1998)

13. Jun-Ying Zhang, I. W. Boyd: Appl. Phys. Lett **71** (20), 2964 (1997)

14. A. G. Grigoryants, *Basics of Laser Material Processing* (Mir Publishers, Moscow, 1994)

15. A. El-Habachi, K. H. Schoenbach: Appl. Phys. Lett. **73** (7), 885 (1998)

16. A. El-Habachi, K. H. Schoenbach: Appl. Phys. Lett. **72** (1), 22 (1998)

17. D. Lindau, H. F. Döbele: Rev. Sci. Instrum, **59** (4), 565 (April 1988)

18. M. Yoshimoto, K, Takubo, M. Komoda, H. Matsunami: Appl. Surf. Sci **79/80**, 264-269 (1994)

19. Y. I. Nissim, J. M. Moison, F. Houzay, C. Licoppe, M. Bensoussan: SPIE **1393**, 216 (1990)

20. V. Craciun, A. Srivastave, J. M. Howard, R. K. Singh, J. Perriere: Appl. Phys. A **69** [Suppl.], S787 (1999)

21. A. Srivastava, V. Craciun, J. M. Howard, R. K. Singh: Appl. Phys. Lett. **75** (19), 3002 (1999)

22. A. Kazor, I. W. Boyd: Appl. Phys. Lett. **63** (18), 2517 (1993)

23. P. Bergonzo, P. Patel, I. W. Boyd, U. Kogelschatz: Appl. Surf Sci. **54**, 424-429 (1992)

24. P. Bergonzo, I. W. Boyd: Appl. Phys. Lett. **63** (13), 1757 (1993)

25. J-Y. Zhang, I. W. Boyd: Electr. Lett. **32** (22), 2097 (1996)

26. J-Y. Zhang, I. W. Boyd: Appl. Phys. Lett. **77** (22), 3574 (2000)

27. J-Y. Zhang, B. Lim, I. W. Boyd, V. Dusastre: Amer. Inst. Phys. **73** (16), 2299 (1998)

28. J-Y. Zhang, I. W. Boyd: J. Appl. Phys. **80** (2), 633 (July 1996)

29. I. W. Boyd: Mater. Sci. Forum **173/174**, 81-92 (1995)

30. S. Kubodera, M. Kitahara, J. Kawanaka, W. Sasaki, K. Kurosawa: Appl. Phys. Lett. **69** (4), 452 (1996)

31. R. S. Taylor, K. E. Leopold, K. O. Tan: Appl. Phys. Lett. **59** (5), 525 1991

32. C. Manfredotti, F. Fizzotti, M. Boere, G. Piatti: Appl. Surf. Sci. **69**, 127 (1993)

33. J. Flicstein, Y. Vitel, O. Dulac, C. Debauche, Y. I. Nissim, C. Licoppe: Appl. Surf. Sci. **86**, 286-293 (1995)

34. O. B. Postel, M. A. Cappelli: Appl. Phys. Lett. **76** (5), 544 (2000)

35. A. Yokotani, N. Takezoe, K. Kurosawa: Appl. Phys. Lett. **69** (10), 1399 (1996)

36. J. D. Ampetepe, J. Diggs, D. M. Manos, M. J. Kelley: J. Appl. Phys. **85** (11), 7505 (1999)

37. J-Y. Zhang, S. L. King, I. W. Boyd, Q. Fang: Appl. Surf. Sci. **109/110**, 487-492 (1997)

38. J-Y. Zhang, H. Esrom, I. W. Boyd: Appl. Surf. Sci. **96-98**, 399-404 (1996)

39. J-Y. Zhang, I. W. Boyd, H. Esrom:Surf. & Interface Anal. **24**, 718-722 (1996)

40. J-Y. Zhang, I. W. Boyd: Electr. Lett. **33** (10), 911 (1997)

41. A. Kazor, I. W. Boyd: Appl. Surf. Sci. **54**, 460-464 (1992)

42. H. Imai, K. Awazu, M. Yasumori, H. Onuki, H. Hirashima: J. Sol-Gel Sci. & Technol. **8**, 365 (1997)

43. J-Y. Zhang, L-J. Bie, I. W. Boyd: Symp. B, E-MRS Spring Meeting (1997)

44. U. Kogelschatz: Appl. Surf. Sci. **54**, 410 (1992)

45. G. Boehme, *Atlantic Ultraviolet Corporation Brochure* (Hauppauge, New York, 1996)

46. B. Eliasson, P. Erni, M. Hirth, U. Kogelschatz: United States Patent 4,837,484 (1989)

47. M. Aguilar-Frutis, M. Garcia, C. Falcony: Appl. Phys. Lett. **72** (14), 1700 (1998)

48. B. H. Lee, Y. Jeon, K. Zawadzki, W-J Qi, J. Lee: Appl. Phys. Lett. **74** (21), 3143 (1999)

49. V. Craciun, R. K. Singh: Appl. Phys. Lett. **76** (14), 1932 (2000)

50. B. K. Moon, C. Isobe, J. Aoyama: J. Appl. Phys. **85** (3), 1731 (1999)

51. A. Yokozawa, A. Oshiyama, Y. Miyamoto, S. Kumashiro: IEEE IEDM 97-703 (1997)

52. S. Maruno, T. Kuroiwa, N. Mikami, K. Sato, S. Ohmura, M. Kaida, T. Yasue, T. Koshikawa: Appl. Phys. Lett. **73** (7), 954 (1998)

53. Y. Matsui, K. Torii, M. Hirayama, Y. Fujisaki, S. Iijima, Y. Ohji: IEEE Electron Dev. Lett. **17** (9), 431 (1996)

54. D. Kumar, J. Sankur, K. G. Cho, V. Craciun, R. K. Singh: Appl. Phys. Lett. **77** (16), 2518 (2000)

55. H. Wengenmair, J. W. Gerlach, U. Preckwinkel, B. Stritzker, B. Rauschenbach: Appl. Surf. Sci. **99**, 313 (1996)

56. C.R. Brundle, C. A. Evans, S. Wilson: *Encyclopedia of Materials Characterization* (Butterworth-Heinemann, Boston, 1992)

57. *CRC Handbook of Chemistry and Physics*, 78th ed., edited by D. R. Lide (CRC Press, Boca Raton, 1997)

58. D. A. Neumayer and E. Cartier, J. Appl. Phys. **90**, 1801 (2001)

59. W. S. Lau, *Infrared Characterization for Microelectronics* (World Scientific, Singapore, 1999)

60. *Handbook of X-ray Photoelectron Spectroscopy*, edited by J. F. Moulder, W. F. Stickle, P. E. Sobol, and K. D. Bomben Physical Electronics, Inc. (Eden Prairie, Minnesota, 1986)

61. H. Ono, Y. Hosokawa, T. Ikarashi, K. Shinoda, N. Ikarashi, K. Koyanagi, and H. Yamaguchi, J. Appl. Phys. **89**, 995 (2001)

62. t. j. Vink, R. G. F. A. Verbeek, J. H. M. Snijders, and Y. Tamminga, J. Appl Phys. **87**, 995 (2001)

63. V. Craciun, J. M. Howard, N. D. Bassim, and R. K. Singh, Mater. Res. Soc. Symp. Proc. **666** (2002)

64. V. Craciun, J. M. Howard, N. D. Bassim, and R. K. Singh, Appl. Surf. Sci. **168**, 123 (2000)

BIOGRAPHICAL SKETCH

Joshua Michael Howard was born July 8th, 1975, in Park Ridge, Illinois. He grew up in Crystal Lake, Illinois, a small northwest suburb of Chicago. Upon graduation from Crystal Lake Central High School in 1993, he began an undergraduate curriculum at the University of Missouri-Rolla in Ceramic Engineering. In 1997, after completing a bachelor of science in Ceramic Engineering and a minor in Spanish, Joshua moved to Gainesville, Florida, to begin his graduate career at the University of Florida in the Department of Materials Science and Engineering. He joined Dr. Rajiv K. Singh's research team in the spring of 1998, and began a project to develop a novel high intensity excimer based vacuum ultraviolet radiation source and then apply the technology to pulse laser deposition of high dielectric constant thin films on silicon. He received his master's degree in 1999 and continued on in pursuit of a PhD. Post graduation plans include working as a post doctoral researcher with Dr. Singh on additional excimer based studies.

I certify that I have read this study and that in my opinion it conforms to acceptable standards of scholarly presentation and is fully adequate, in scope and quality, as a dissertation for the degree of Doctor of Philosophy.

Rajiv K. Singh, Chairman
Professor of Materials Science and Engineering

I certify that I have read this study and that in my opinion it conforms to acceptable standards of scholarly presentation and is fully adequate, in scope and quality, as a dissertation for the degree of Doctor of Philosophy.

Stephen J. Pearton
Professor of Materials Science and Engineering

I certify that I have read this study and that in my opinion it conforms to acceptable standards of scholarly presentation and is fully adequate, in scope and quality, as a dissertation for the degree of Doctor of Philosophy.

Cammy Abernathy
Professor of Materials Science and Engineering

I certify that I have read this study and that in my opinion it conforms to acceptable standards of scholarly presentation and is fully adequate, in scope and quality, as a dissertation for the degree of Doctor of Philosophy.

David P. Norton
Associate Professor of Materials Science and Engineering

LD
1780
2002
.H849

UNIVERSITY OF FLORIDA
3 1262 08555 3435